
Defect Tolerance In Fabrication Of High Transmission Diamond Nanotextured Moth-Eye Surfaces For Near-IR Application

Author:

Jordan Moshcovitis

Supervisors:

Steven Prawer

*Submitted as partial fulfilment of the requirements for the degree
of Master of Science*



UNIVERSITY OF MELBOURNE

SCHOOL OF PHYSICS

February 28, 2022

Acknowledgements

Without the assistance of numerous close friends and colleagues, it would have been impossible to complete this thesis. Finally, I would like to express my sincere thanks to Prof. Steven Prawer for accepting me as a student and his ongoing support and guidance throughout my degree.

I would also like to express my gratitude to the following former and current members of the Cybernetics research group: James Belcourt, Drs. Athavan Nadarajah, Stella Aslanoglou, and David Garrett have all aided me in my research and provided invaluable insights, for which I am always grateful.

Additionally, I have been fortunate to share an office with fellow students who have contributed to making my time here enjoyable: Andre Chambers and Sachin Shajil, have created an environment that is supportive, welcoming, and intellectually stimulating throughout my degree. There are those also outside the office who made the time more meaningful: Ran, Theo, Alex, Barney, David, Marcello, and Mozdeh.

Outside of direct research assistance, I would like to thank Assoc. Prof. Jeff McCallum and Poppy Gatsios for their continued support and assistance on a number of occasions over the last two years.

This research was supported by The University of Melbourne's Research Computing Services and the Petascale Campus Initiative.

Statement of Contribution

I, Jordan Moshcovitis, declare that this thesis titled, "Defect Tolerance In Fabrication Of High Transmission Diamond Nanotextured Moth-Eye Surfaces For Near-IR Application" and the work presented in it is my own unless otherwise specified. The following parts of this work were undertaken in collaboration with others:

- Samples 2,3,4,5 and validation samples and measurements used in this work were fabricated and collected by James Belcourt from the School of Physics, the University of Melbourne from previous work.
- Atomic force microscopy was performed by Dr Athavan Nadarajah from the School of Physics, University of Melbourne.
- Scanning electron microscopy was performed with the assistance of Dr Stella Aslanoglou from the School of Physics, University of Melbourne.
- The fabrication of diamond moth-eye textured surfaces described were performed with the assistance of Dr Athavan Nadarajah and James Belcourt from the School of Physics, the University of Melbourne, using a process that he developed.

.....
Jordan Moshcovitis

Abstract

Nano-textured optical surfaces have found widespread application in many fields. Using a gradient refractive index (GRIN), anti-reflective (AR) surfaces are widely employed to minimise the Fresnel reflection losses. Diamond nanophotonic devices provide several physical advantages when used as optical windows for microelectronics and advanced biomedical devices. High hardness, wideband transparency, high thermal conductivity, chemical inertness, and biocompatibility are all characteristics of diamond windows. These characteristics make them ideal for applications such as lasers, optics, plasma physics, and implantable devices. However, the high refractive index of diamond results in large losses due to reflection. Fabrication of moth-eye structures on diamond substrates is an attractive approach to reduce their surface reflectivity. Compared to standard anti-reflective chemical coatings, the anti-reflective biologically inspired moth-eye structure demonstrates outstanding low reflectivity and high transmission even for wide-angle incidence and over a wide range of incident wavelengths.

The surface structures studied here are composed of regular arrays of protuberances that reduce reflections at the air-substrate interface. However, the techniques used to fabricate these structures often induce various types of topological defects, which degrade their optical properties. Thus, a critical parameter in determining the robustness of diamond moth-eye surfaces is the sensitivity of transmission to deviations in ideal moth-eye surface topologies.

In this work, we employ finite element simulation and numerical modelling to analyse the effects of particular non-uniform defect features on the diamond moth-eye surface. As a basis for simulations, defect-mediated model patterns were generated with properties extracted from scanning electron and atomic force microscope images of fabricated samples. Using surface morphology statistics from atomic force microscopy and scanning electron microscopy characterisation, the effective transmission of the diamond moth-eye surface with defects was estimated using the finite element method. We report statistical tolerances for the dominant geometrical features that influence the effective transmittance for normal incident light of a wavelength of 850nm . This wavelength is of particular interest for biological applications in which diamond windows encapsulate electronics. Numerical procedures were used to identify the geometry for optimal transmission, which was found to be a height of 500nm with a spacing of 150nm for the pillars. We found that the transmittance of the surface was most sensitive to variations in the radius of the pillars and the surface roughness. Surprisingly, the transmittance was found to be relatively insensitive to missing pillars; up to 50%, of the pillars can be missing without a significant reduction in transmission. The transmission was also found to be quite insensitive to some other spatial disorder types. A predictive general model was developed based on simulations and verified with experimental data for morphological and topological defect surfaces. We conclude that the most important defect to minimise is the roughness due to etching-related defects. It appeared to be the most dominant and important to minimise comparatively, rather than the precise ordering of the pillars. Finally, potential directions for future research are proposed, such as an extension to alternative modelling approaches and investigation parameters of the etching technique, which most significantly influence the surface roughness, which in turn degrades the transmission.

Contents

Acknowledgements	i
Statement of Contribution	i
Abstract	ii
1 Introduction	1
1.1 Moth-eye anti-reflective nano-textured diamond photonic surfaces	3
1.2 Defects as a limiting factor to high transmittance	3
1.3 Scope and objectives	4
2 Background	5
2.1 Theory of anti-reflection phenomena	5
2.1.1 Anti-reflective coatings	5
2.1.2 Graded refractive index coating	6
2.1.3 Nanostructured surfaces	6
2.2 Moth-Eye anti-reflective surfaces	8
2.2.1 Optical Properties	8
2.2.2 Moth-eye surface simulations	9
2.3 Fabrication of and defects on moth-eye surfaces	10
2.3.1 Defects in moth-eye diamond surfaces due to LB and RIE fabrication	11
2.3.2 Studies of defect tolerance and sensitivity	13
2.4 Summary	13
3 Methods	14
3.1 Modelling simulation tools and procedure	14
3.1.1 Assumptions for the model	14
3.1.2 Simulation pipeline	15
3.2 Model description	16
3.2.1 <i>COMSOL</i> specification of the close-packed moth-eye surface	17
3.2.2 Geometry and boundary conditions	18
3.3 Defect generation	20
3.3.1 <i>MATLAB</i> defect simulation approach	20
3.3.2 Inclusion of SEM and AFM data in defect generation	21
3.3.3 Defect parameters and surface generation	21
3.3.4 Fabrication and characterisation of diamond moth-eye surfaces	25
3.4 Gaussian Process Regression	26
3.5 Summary	27
4 Results	28
4.1 Parameter space search for the ideal surface geometry	28

4.1.1	Discussion: Transmittance near region of ideal pillar geometry	30
4.1.2	Deviation from the ideal geometry and effect on the transmittance	31
4.2	Transmission sensitivity to simulated random defects	33
4.2.1	Topological defects	33
4.2.2	Profile curvature and random roughness	35
4.3	Discussion: Transmission sensitivity to statistical deviation	36
4.4	Comparison of Simulation with Experiment	39
4.5	Summary	41
5	Conclusion	42
	Bibliography	44
	Appendix	45
A	Finite element modelling	46
B	Defect Metrics	47
C	Machine Learning Model	48
D	Sensitivity of transmittance to defect metrics	49

Chapter 1

Introduction to nano-textured diamond photonic surfaces

Nano-scale texturing forms a significant part of modern optical systems technology. Surface texturisation enhances light absorption in photovoltaics, optical sensing devices, and flexible displays. In particular, textured anti-reflective surfaces (ARS') offer a significant advantage over standard thin-films, or multi-layer films designed to reduce reflections [1, 2, 3]. Material-mediated controlled propagation of light is finding growing commercial interest, especially in the interaction of light with artificial media composed of sub-wavelength structures [4, 2, 5]. These media can be fabricated from various materials, including metals, dielectrics, semiconductors, and different combinations thereof. These artificial materials are called metamaterials and can provide optical attributes which are not achievable in natural media [3]. Surface modified diamond is one such material, where surface modification is used to control the microstructure and optimise for optical device applications [6, 7]. Diamond's high breakdown voltage, transparency from ultraviolet to far-infrared (IR), chemical resistance, high laser damage thresholds and high operating temperatures make it highly desirable to use in a variety of conditions and environments but also imposes challenges when seeking to nano-structure the surface [8, 9].

Conventional anti-reflection coatings (ARCs) are designed based on the destructive interference of light from multiple interfaces [10]. ARCs consist of one or more dielectric layers deposited on the surface of an optical substrate with refractive index n between that of the substrate and environment [11]. Thin-film ARC design includes single-layer anti-reflective (SLAR), double layer anti-reflective (DLAR), or multiple-layer anti-reflective (MLAR) structures [12]. MLARs are superior to SLAR coating in attaining broadband transmission, and high angular tolerance [3]. The deposition of layers of uniform films on a bulk substrate is a technique for grading the refractive index of the air to that of the substrate, thereby reducing reflection [1]. The design of these thin-film layers enables the system to reduce reflection within a specific wavelength band through destructive interference of transmitted and reflected light [1]. However, the controllability of film thickness and availability of suitable materials with desirable refractive indices limits the use of this method [13]. In addition, when illuminated by a high power source, the difference between the thermal expansion coefficients of different layers introduces residual stresses [14], affecting mechanical stability [5], high-power infrared laser transmission applications [15] and can lead to delamination of the coating.

As an alternative, nano-structured anti-reflection surfaces (NARSs) exhibit larger working bandwidth, low power loss from reflection, larger acceptance angles and robustness compared to traditional anti-reflection coatings [1]. The variation of a material's density via surface modification techniques, such as photolithography or etching, allow for a graded refractive index to be implemented. By constraining the spatial periodicity, anti-reflective properties can be tailored according to the wavelength of light and substrate material. One advantage of introducing sub-wavelength (SW) texturing is the topological

control of the reflectivity due to the effective refractive index at the surface interface. Thus, the SW structure spacing approximates an optically anisotropic thin film. The intermediate value of n between two media may be controlled by spatial variation of the frequency, depth and shape of the nano-structures [15]. Another crucial advantage of SW texturing compared to microtextured and thin-film coatings is that the anti-reflective properties may exist for a broad spectrum of light at a wider angle of incidence.

NARSs exhibit an adiabatic change of the effective refractive index n in the transition from the incidence medium to that of the substrate [16]. These structures, as shown in Figure 1.1b, are referred to as 'moth-eye' structures due to their resemblance with a moth's eye [17].

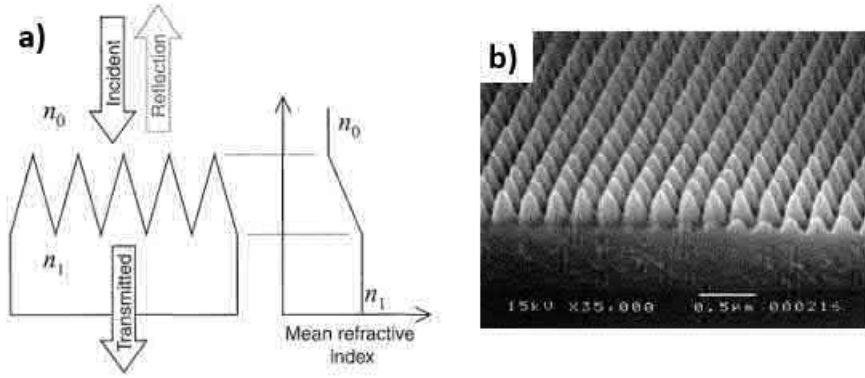


Figure 1.1: **a)** Schematic cross-section diagram of typical ARS. The effective refractive index increases gradually from the refractive index of air n_0 to that of the substrate n_1 [4] **b)** Scanning electron microscope (SEM) image of ARS surface with period 250 nm and height 250 nm. [4].

The moth-eye structure has been developed as a bio-inspired anti-reflection method based on the anti-reflective properties of moth-eyes in nature [13]. The moth-eye is covered with a regular array of periodic protuberances covering the moth-eye's outer surface, wherein the scale of the micro-nano structure is smaller than the incident wavelengths of light. The hexagonal close-packed arrangement of these nano-structures permits incident light to interact with the entire surface in a graded manner instead of resolving each structure unit cell independently [1]. For subwavelength periodicity, the mean refractive index of the moth-eye surface structure changes in the vertical direction, from the air to that of the substrate. Therefore, the waves are primarily unperturbed by this micro-nano structure [18]. The hierarchical architectures comprising an array of highly ordered nanopillars found on the corneal lens surface of the compound eyes of moths and butterflies are natural analogue variants of such graded-refractive index (GRIN) between the interface of the ambient medium and the surface of the eye [3].

Derived from the design of the sub-wavelength surface relief nano-structures, each ommatidium of the moth-eye exhibits excellent AR property within a wide angle of incidence, predominantly known as the 'moth-eye effect' [13]. Furthermore, due to the monolithic geometric morphology and material homogeneity, the moth-eye nano-structures are endowed with superior mechanical stability and durability compared to ARC [5]. Moreover, by satisfying conditions on the thickness, t , of the graded refractive index region, $t \approx \lambda/2$, related morphological variation of the reflectance is reduced to below 0.5% [19].

Establishing a universal method for investigating defects in anti-reflective moth-eye surfaces is highly desirable due to the wide applicability of the moth-eye design. Widespread research efforts have been focused on fabricating moth-eye-inspired GRIN nano-structured arrays for various optical applications such as solar cells [18], light-emitting diodes [20], OLED [21], display screens [22] and most importantly, in microelectronic medical implants [9, 10, 23]. GRIN nano-structures have been fabricated on various materials, including metals, metal oxides, silicon oxides, silicon, polymers, and advanced composite materials [2]. With the development of Laser Interference Lithography (LIL) [2, 3], and accurate characterisation technology of the structures [10], micro-and nano-structures have gradually achieved high precision. However, while these materials provide broadband and omnidirectional anti-reflection capabilities, they suffer from low chemical stability in the physiological environment, which hinder their application in optical devices or as encapsulating materials in optically driven medical implants [9, 23, 24].

1.1 Moth-eye anti-reflective nano-textured diamond surfaces

Diamond is a wide bandgap biocompatible semiconductor exhibiting optical transparency over a broad band of light wavelengths [17]. It is a promising material for integrated photonics, optomechanics, and quantum information processing (QIP) applications [25]. Polycrystalline diamond thin films show a unique combination of physical properties for optical device applications, such as high hardness, transparency from UV to far-infrared (IR), chemical inertness, and high laser damage thresholds [2].

Diamond is an ideal window material for high-power laser applications [26]. However, one limitation is that diamond surfaces encounter strong Fresnel reflection due to a high n value of 2.39, corresponding to reflection losses at a single surface of 17% [20]. A practical solution is provided by patterning the diamond surface using hybrid top-down/bottom-up fabrication technologies, nanolithography, and 2D crystallisation techniques [8]. The use of diamond surface relief structures effectively reduces Fresnel reflection losses of high-index substrates [27]. The fabrication of single-mode anti-reflective devices, such as ‘moth-eye’ surfaces, can be realised in a single-crystal diamond. High transmittance levels and minimal long-wavelength scatter characterise these devices, despite their coarse-grained morphology [7]. Such a biomimetic nano-texturing of diamond is well modelled by the effective medium theory (EMT) approximation [28], which has been successfully applied in the design of a variety of anti-reflective surfaces [2].

In an example application, soft lithography –Langmuir-Blodgett (LB)–, using a monolayer of silica nanospheres, was used to dry-etch patterned nano-structures onto the diamond surface [23]. The resulting moth-eye diamond surface exhibited a broadband transmission enhancement in the range of 600nm to 900nm, with 99.3% transmission at 852nm [23].

1.2 Defects as a limiting factor to high transmittance

The optimal profile shape and the theoretical performance of anti-reflection structures are already known [29]. However, the specific profile form and height of the structures and the position within the unit cell may show a variation over the expanse of the nano-structured area [16]. In addition, the fabrication technology may influence the local topology of the periodic structure to deviate from

that of the repeating unit cell. Consequently, scattering effects increase in the presence of topological imperfections in moth-eye textured surfaces. On the other hand, nanosphere lithography, which combines self-assembly and reactive ion etching techniques, enables the reproducible fabrication of submicron structures over $10mm \times 10mm$ surfaces at a lower cost and with greater scalability than more sophisticated top-down methods [30].

However, vacancies, dislocations, and multi-layer defects are generated from the self-assembly procedure of nanospheres [3, 31, 32]. Imperfections, including the variations in the lateral spacing between single protuberances, lead to noisy spatial correlation associated with diminished anti-reflective properties and zeroth-order diffraction. In addition, etching-induced roughness of the order of $30nm$ may affect local stability when roughness corresponds to flatter-topped pillars, evidenced by variation between conical and cylindrical structure shapes [16, 33]. Although researchers [18, 20] have considered limitations in the control of lattice spacing and texturing, few studies have been performed to examine the effect of variations in moth-eye structure morphology, and surface topology on their anti-reflective properties [20].

1.3 Scope and objectives

The goal of the research presented in this thesis is to systematically analyse the effect of defects in texture on the transmittance of the moth-eye surfaces on diamond. The surfaces are designed to be used in high transmission optical windows operable under wavelength $\lambda = 850nm$ [9]. Experimental moth-eye diamond samples fabricated using nano-lithographic Langmuir-Blodgett and reactive-ion etching (RIE) methods motivate the selection of the defects investigated and qualify the numerical simulations' accuracy. While this method of fabrication is less precise than conventional E-beam lithography, it has several advantages over top-down sequential methods in terms of speed, affordability, high throughput, and scalability [34]. However, morphological and topological errors introduced during this fabrication method (see Figure 2.8) degrade the optical properties of moth-eye surfaces. Therefore, it is important to characterise these effects, and the impact on transmittance, to guide further development using nano-textured diamond as a highly stable sub-wavelength broadband ARS. We use *COMSOL* and *MATLAB* numerical simulations at multiple length scales to quantify the degree of variation allowed on the nano-textured surface that would still maintain highly efficient AR properties. Finally, based on the previous analysis, a model is proposed to simulate the non-ideal surface characteristics and identify relevant transmission loss mechanisms in the nano-textured biomimetic diamond-based ARS.

The objectives achieved in this research work are as follows:

1. The analysis of anti-reflection attributes of moth-eye type nano-structured ARS's.
2. The study of fabricated anti-reflective nano-structure patterns and the derivation of high-transmission conditions from design tolerances of the moth-eye nano-pattern.
3. The implementation of simulations and numerical modelling to determine the sensitivity and robustness of the anti-reflective efficiency of moth-eye diamond surfaces with and without defects.
4. The development of a theoretical method to predict the efficiency of diamond moth-eye surfaces extracted from SEM and AFM image analysis

Chapter 2

Nano-textured ARS: Theory and experiment

2.1 Theory of anti-reflection phenomena

Ideal ARC surfaces exhibit surface layers with a gradually decreasing refractive index. An incident wave is partially reflected when it crosses the boundary of two media with different refractive indices. According to Fresnel reflection, the difference in refractive indexes of the two consecutive surfaces should be small to generate a series of reflections; otherwise, loss from reflection can be significant at normal incidence. Without an AR layer, the Fresnel reflection coefficient R and transmission coefficient T of incident light at normal incidence are given by [5]:

$$R = \left(\frac{n_1 - n_2}{n_1 + n_2} \right)^2 \quad T = \frac{4n_1n_2}{(n_1 + n_2)^2} \quad (2.1)$$

where n_1 and n_2 are the refractive indices of the first and second medium respectively. If n changes gradually, the reflectance can be considered the consequence of an infinite series of reflections at each incremental change in the refractive index.

AR coatings are a common technique for coating purposes in industry. These coatings are equally effective at operating at a single wavelength (for narrowband lasers) as they can be designed to operate over extremely broad spectrum bands ($380nm - 1550nm$ or $3\mu - 12\mu m$). The relationship between reflectance, refractive index, layer thickness, and design is critical in determining when modern ARC technology should be used. The applications of ARC's are primarily determined by the wavelength or multiple wavelength spectra required for a particular application.

2.1.1 Anti-reflective coatings

High reflectance at interfaces can be overcome by incorporating intermediate index materials (single or multilayer) that reduce interference reflectance for specific film thicknesses, incident wavelengths, and incidence angles [5]. As illustrated in Figure 2.1a, single layer thin films operate on the principle of destructive interference between multiple light reflections from the film's top and bottom surfaces, and their control is determined by the optical path difference within the film. Following the deposition of a single-layer dielectric thin film with a refractive index of n on a substrate with a refractive index of n_s , two distinct interfaces are formed, resulting in two reflections. AR properties can be obtained when destructive interference occurs between two reflections due to their phase difference. This is enhanced by the deposition of multiple thin layers of dielectric materials on the external surface of the window or optic in a thin film stack, as shown in Figure 2.1b [14]. Each material layer is optimised to cause destructive interference at a particular wavelength reflected from the window or optical surface, such that the overall effect is for the surface to appear transparent.



Figure 2.1: Propagation of light through **a)** a substrate with a single layer film ($n_s > n$) and **b)** a substrate with a multilayer film and stepped refractive index profile.

The resultant reflection vector can be expressed as [5]:

$$R_{sum} = R_1 + R_2 + R_3 \quad (2.2)$$

A state of anti-reflection can be achieved by minimising the value of R_{sum} . This state can be obtained by changing the refractive index and film thickness of each layer in accordance with the thicknesses of the other layers.

2.1.2 Graded refractive index coating

An alternative way to minimise the reflectivity is to use an inhomogeneous film with a gradually decreasing refractive index. Graded refractive index (GRIN) surfaces have been investigated for broadband, and omnidirectional AR performance [28]. The optical behaviour of incident light reflected at a surface coated with a homogenous thin layer, and inhomogeneous graded index layer is illustrated in Figure 2.2. The reflection reduction occurs when the difference in the refractive indices between the substrate and air is minimised. This step is known as optical impedance matching. Obtaining a layer in GRIN structures with a perfectly matched index and optical impedance from the substrate to the air is challenging. Typically, there is also a gap between the GRIN ARC's top surface and the surrounding air's refractive index (~ 1.05 and ~ 1 , respectively). Additionally, a refractive index mismatch frequently develops at the coating-substrate interface, as the absorbent substrate has a complicated n [28].

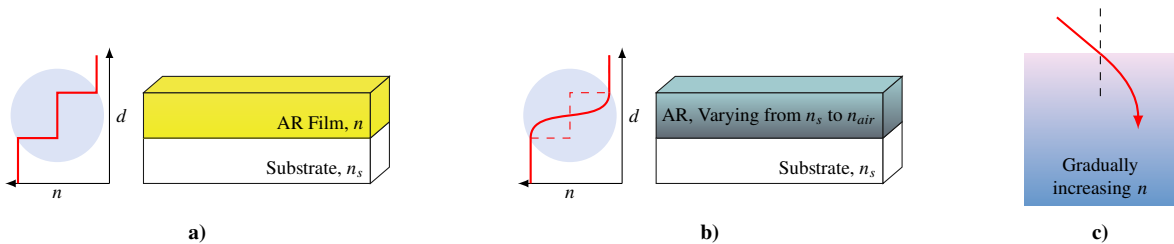


Figure 2.2: Schematic comparison of homogeneous and inhomogeneous ARCs. **a)** A sharp decrease of n observed in single layer ARC **b)** smooth depth-dependent decrease of n in case of GRIN coating **c)** bending of light ray passing through the GRIN medium. [5]

2.1.3 Nanostructured surfaces

Another anti-reflection method inspired by nature is based on biomimetic nanostructures (NS) [22]. The use of nano-structured materials improves the robustness of AR performance compared to con-

ventional AR coatings [10]. These AR nano-structured surfaces must adhere to a stringent criterion: subwavelength mixing of the substrate material with the surrounding air [10]. A GRIN profile is created by utilising a homogeneous nano-structured material, which minimises reflections. Nano-structured surfaces can be patterned in a variety of different geometries that affect how the effective medium transitions from, n_{air} to n_s (Figure 2.3). Following that, the profile shape, depth and spacing can determine the final optical properties.

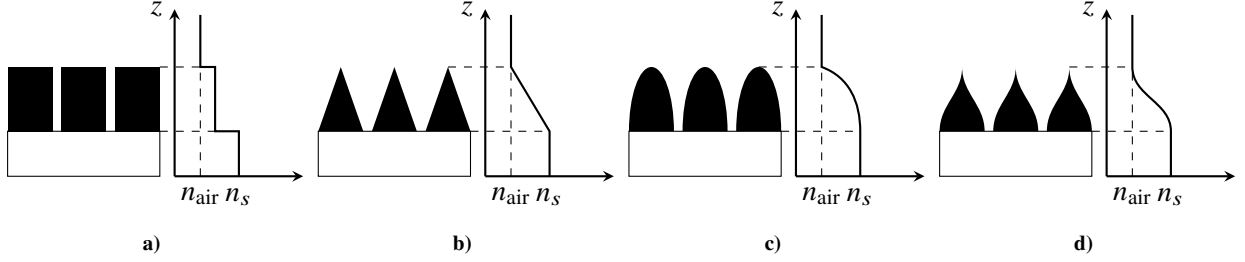


Figure 2.3: The effect of the nano-structure shape on the gradient of n between two media. **a)** Inserting a material of equal thickness and with an intermediate refractive index produces a zero-step gradient. **b)** Inserting a material with a linearly graded refractive index between air and the substrate produces a linear gradient. **c)** and **d)** have a curved gradient which has a similar effect to **b)** with the exception that the gradient of the refractive index is non-linear [35].

There are two distinct methods for obtaining AR properties, which vary in their application depending on the characteristic scale of the structure arrays, d , and the wavelength of the incident light, λ . If $d \gg \lambda$, the surface appears as a diffraction grating, with angle-dependent reflection. In the opposite case, $d \ll \lambda$, the surface can be described as a gradient-index material. These different optical regimes are represented and explained qualitatively in Figure 2.4 [17].

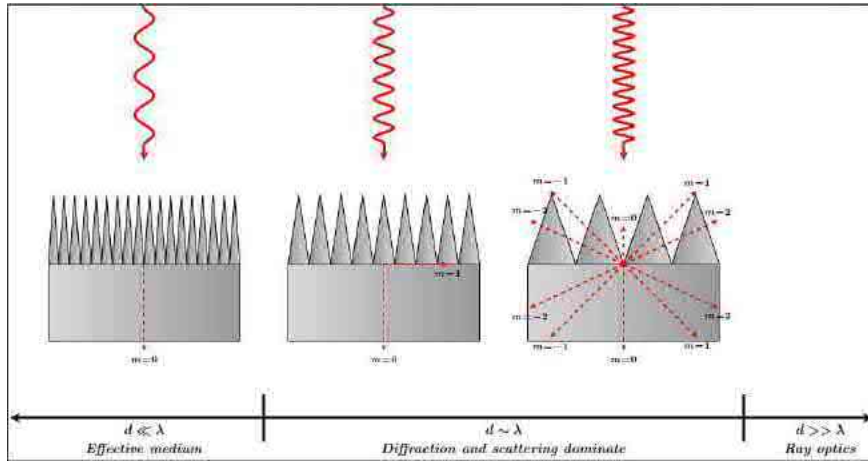


Figure 2.4: Schematic of optical regimes associated with different structure sizes depending the scale of the wavelength λ as smaller, of the same order, or infinite compared to a characteristic length scale, d , of the surface texture (feature size and periodicity) demonstrating that effective medium theories apply to structures with periods, p , significantly smaller than the wavelength of light λ [15]. Different diffraction orders are denoted by m .

As a result, if the unit scale of the structural arrays, d , is smaller than the wavelength λ , incident light is insensitive to the individual structure and bends gradually due to graded refractive index changes, as illustrated in Figure 2.5. Since array features are subwavelength of the incident light, incoming photons interact with an effective medium whose optical properties are intermediary to those of the media on either side of the interface [2].

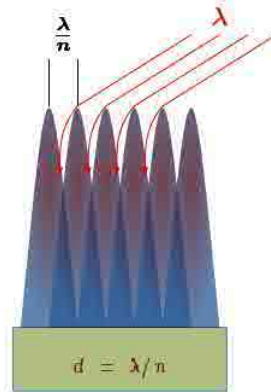


Figure 2.5: Light trapping on subwavelength textured surface given subwavelength condition where spacing d equals $\frac{\lambda}{n}$.

2.2 Moth-Eye anti-reflective surfaces

2.2.1 Optical Properties

Certain moth species are covered in an array of tapered pillars that extend from their eyes and wings. The investigation of these corneal nipple arrays in moth-eyes resulted in the creation of effective AR solutions in the form of 'moth-eye' AR schemes. Moth-eye ARSs can be considered a highly effective AR medium composed of a uniform distribution of low-index gaps and high-index pillars. Moth-eye ARSs are crystalline microstructures comprised of an irregular or regular hexagonal array of conical nipples that suppress reflection over a broader wavelength and incidence angle range than multilayer dielectric ARCs. The moth-eye structure has several advantages over conventional thin-film ARCs, including increased environmental endurance, minimal surface preparation, improved surface adhesion, single-material production, self-cleaning (lotus effect), and a higher threshold for laser-induced damage. Figure 2.6 shows the eye of the moth (left) and an SEM of the same eye. SEM reveals the fine structure patterns with a unit scale smaller than the wavelength.

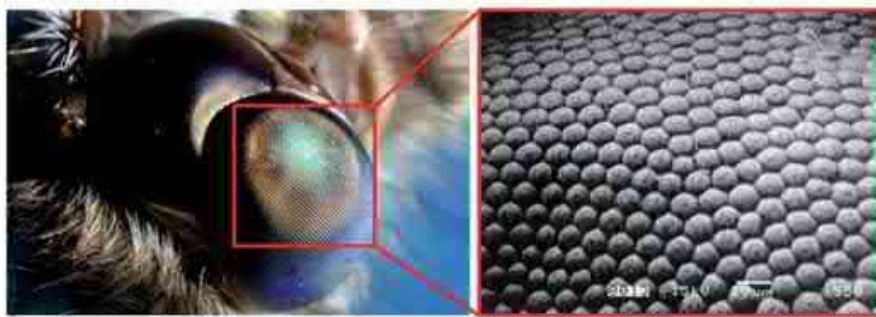


Figure 2.6: (Left) The eye of a moth and a SEM image of the same showing the protuberances on the outer surface of the corneal lens (Right)[5].

Synthetic moth-eye structures with subwavelength tapered features replicate an inhomogeneous surface with an axially varying refractive index, which results in adiabatically varying impedance matching and thus reflection suppression. The absence of a sharp change in the refractive index ensures that light is transmitted through the interface into the substrate medium without reflection. As a result, the tapered profile behaves as if an infinite number of infinitesimally thin layers are stacked on the surface as illustrated in Figure 2.7 [22].

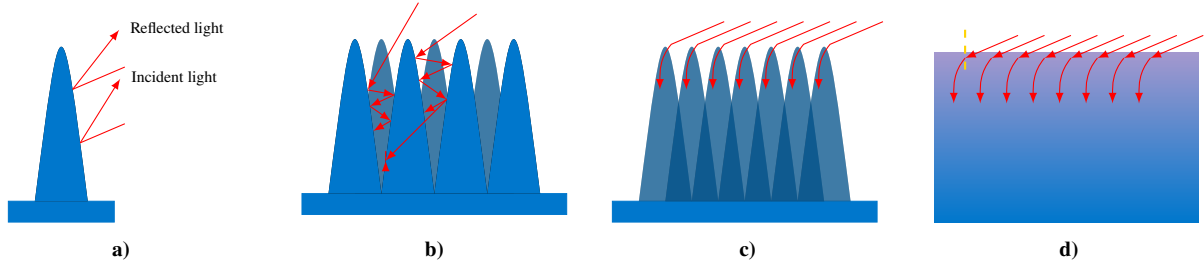


Figure 2.7: **a)** Interaction of light with macrostructure. **b)** Multiple internal reflections occurred as a result of the arrays of microstructures. **c)** Interaction of light with a nanostructure array. **d)** Interaction of light with the GRIN structure results in the bending of light rays [13].

The refractive index of a smooth tapering nanostructure in the z -direction results in a gradual change in the effective n between the two media of the interface, allowing for improved transmission [22]. This is the underlying principle of effective medium theory (EMT), also known as homogenisation [36]. The effective refractive index is proportional to the relative amounts of each medium in each layer, as governed by the profile of the graded index region [16]. If the layer is composed of a non-dispersive medium with impedance matching only at a specific frequency, it acts as a monochromatic anti-reflection layer without a constraint on thickness and allows for complete transmission of light [2]. The AR property of moth-eye surfaces is determined by the scale of the surface texture in relation to the incident light wavelength. Thus, moth-eye features are frequently of a scale just below the wavelength of incident light. When the spacing between the structures is significantly less than the incident wavelength, and the depth of the structures is large, the moth's eye texture is optimal.

The AR properties of moth-eye nano-structured arrays are relatively independent of wavelength, angle of incidence and polarisation due to the bending of incident rays by the gradient index surface. The refractive index gradually changes for non-normal angles of incidence, which can suppress broadband reflection [4]. Because the polarisation-dependent transmission is independent of media with extremely low refractive index disparity, light with p - and s -polarization can be reduced significantly [37]. As a result, sub-wavelength nanostructures with graded refractive index changes can achieve broadband, omnidirectional, and polarization-insensitive AR properties.

2.2.2 Moth-eye surface simulations

Due to the difficulty and impracticality of perfect structure fabrication, modelling AR sub-wavelength structures is a significant field of study [38]. Among the numerous modelling techniques available, the transfer matrix method (TMM), the rigorous coupled-wave analysis (RCWA) or Fourier modal method (FMM), the finite-difference time-domain (FDTD) method, and the finite element method/analysis (FEM/A) are the most frequently used in the field of optical modelling for AR coatings [12]. These techniques are considered to provide precise and rigorous solutions to Maxwell's equations [36]. The dimensions, shape, period, and location of subwavelength structures and material parameters such as the permittivity and permeability for bulk materials and surface features are used as inputs to ARS reflectivity simulations [36]. Over the last decade, significant progress has been made in linking classical Maxwell's equations to other well-known modelling methods, particularly in the field of nanoscale plasmonic and optical property prediction [36].

2.3 Fabrication of and defects on moth-eye surfaces

Nano-textured AR surface implementations provide a relatively simple, scalable, and controllable method for designing the AR surface's spectral reflection [17]. Numerous lithographic techniques have been extensively used to create nano-structured surfaces. However, top-down techniques are prohibitively expensive to implement and require sophisticated equipment. Bottom-up colloidal self-assembly fabrication is a much simpler and more cost-effective method than nanolithography for fabricating a wide variety of periodic nanostructures. In this method, nanoparticles are deposited on the surface and act as the etching mask through which hexagonally or stochastically ordered pillars are formed [39]. Traditional self-assembly produces colloidal crystals that are hexagonally ordered. Unfortunately, current colloidal templating technologies have a low throughput and are incompatible with mature microfabrication, making practical devices challenging to mass-produce. Monolayer colloidal arrays can be used as etching masks in conjunction with standard RIE processes to create broadband moth-eye anti-reflection surfaces on a variety of substrates.

Self-assembly with nanosphere lithography (NSL) can be used to fabricate moth-eye nanopillars on a substrate in a densely packed structure [30]. NSL is a cost-effective manufacturing process that produces a uniformly textured surface. The advantages of bottom-up and top-down approaches are combined in this process. The colloidal NSL process is centered on the formation of a densely packed monodisperse monolayer mask of nanospheres, typically polystyrene or silica, on the liquid-air surface [39]. There are numerous variants of the monolayer formation technique. These processes include evaporative assembly, spin coating, Langmuir-Schaefer, and Langmuir-Blodgett deposition [34]. The procedure is divided into two stages. The first step is to prepare the monolayer mask, and the second step is to etch. To prepare the mask, at the fluid-fluid interface, the monodispersed charged colloids are generally arranged in a monolayer of crystalline order. The nanospheres' high surface area to volume ratio and strong Coulomb interactions enable them to form highly dense hexagonal surface distributions with an average periodicity equal to their diameter. The water level is then decreased to allow the dense monolayer to adhere to the substrate. Once the water solution has dried, this monolayer may be used directly as an etch mask for the substrate [35]. The reactive-ion etching (RIE) process is then found to have a significant effect on the surface morphology of AR nanostructures [15, 21]. RIE is used to create the substrate's morphological properties, and the final surface texture [15].

It is important to consider the imperfections and defects inherent in moth-eye ARSs in general and the defects introduced by bottom-up lithographic technologies. Moth-eye surfaces with irregular defects that are randomly distributed are typically based on a self-organised pattern with a natural period determined by the underlying formation phenomena. Numerous process parameters influence the deposition uniformity, including ambient humidity, temperature, microsphere concentration, substrate surface energy, and the presence of additional polymers in the nanosphere lithographic process [39, 40]. As a result, random-textured nanostructures with non-uniform topology and morphology emerge [41].

For random moth-eye surfaces, and moth-eye surfaces in general, the quality of the surface texture and consequentially, the efficiency as an AR surface depend on two factors [15]:

- Monotonic decrease of refractive index from external medium to substrate.
- Smooth transition of refractive index at boundaries

In manufacturing processes, stochastic uncertainties associated with fabrication variations related

to design geometry, material composition and surface quality are inherent [41]. Furthermore, it is well known that such uncertainties can dramatically impact the functionality of fabricated device surfaces [32]. As discussed in Section 2.2, the performance of index matching moth-eye surfaces, assuming that the material is homogeneous and the texture is regular, is determined by the shape and periodicity of the moth-eye structure. However, a perfect surface is seldom achieved by self-assembly procedures over the entire substrate [35]. Moreover, the self-assembly process has a degree of uncertainty and its results vary with each application [32]. Therefore, to achieve a high-quality design of an optical device surface, such uncertainties must be considered early in the design process. Consequently, uncertainty quantification approaches have become critical tools for rapidly obtaining statistical information about AR surfaces and achieving high-quality design [42].

2.3.1 Defects in moth-eye diamond surfaces due to LB and RIE fabrication

The large-area diamond moth-eye surfaces are fabricated by depositing a sacrificial mask of silica nanospheres on a diamond substrate, via Langmuir-Blodgett film, followed by RIE to create the moth-eye texture. The use of LB in conjunction with RIE introduces multiple defects in ideal surface texture resulting in a decrease in transmittance [23]. Generally, the fabrication process (Figure 2.8) is affected by various parameters [21, 22], viz, the aspect ratio of the nanostructures, the shape of the pillars or the shape and size of the nanoparticles used on the surface layers, the inter-pillar spacing or distance between nanoparticles, and the type of material used to prepare the colloidal assembly.

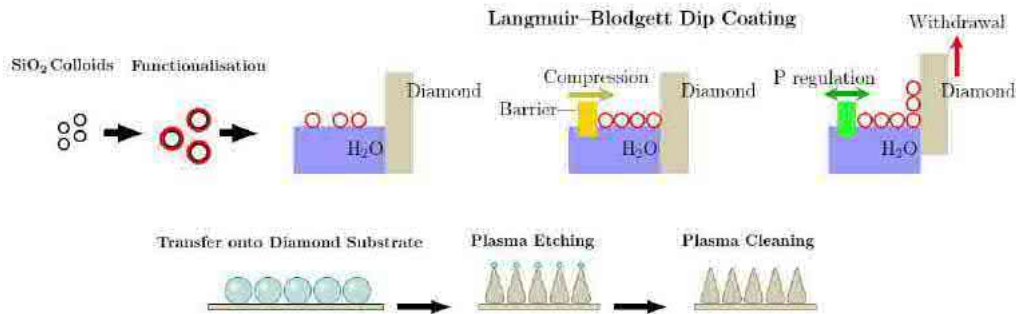


Figure 2.8: A process flow for fabrication of moth-eye surfaces on diamond. Functionalised SiO_2 colloidal solution is suspended on the water surface and compressed in the Langmuir-Blodgett trough to form a densely packed monolayer template. Prior to deposition, the diamond surface is treated to be hydrophilic. The diamond substrate, coated with the SiO_2 mask, is then removed from the trough while the surface pressure is regulated. Transfer of the pattern is accomplished via RIE etching, and the mask is removed via wet or dry etching [34].

Structural deviation from the perfect moth-eye surface will almost certainly affect the size of the inter-pillar spacing. This deviation manifests itself in the form of overall surface roughness and misalignment of the fundamental elements as presented in Figure 2.9. Since the surface, as described in Section 2.3, may be easily fabricated using templates, fabrication occurs in stages. While the position of the fundamental elements, as well as their shape and dimension, can be precisely controlled at each stage, maintaining consistency between stages is more complex, and although variation is mitigated by design, it still impacts performance [43]. In general, researchers have examined the following disorders associated with fabrication:

- Variations in the packing of the surface
- Variation in the height of structures

- Localised structural misalignment
- Inaccuracy in fabricating the aspect ratio of the structure
- Roughness of the overall surface

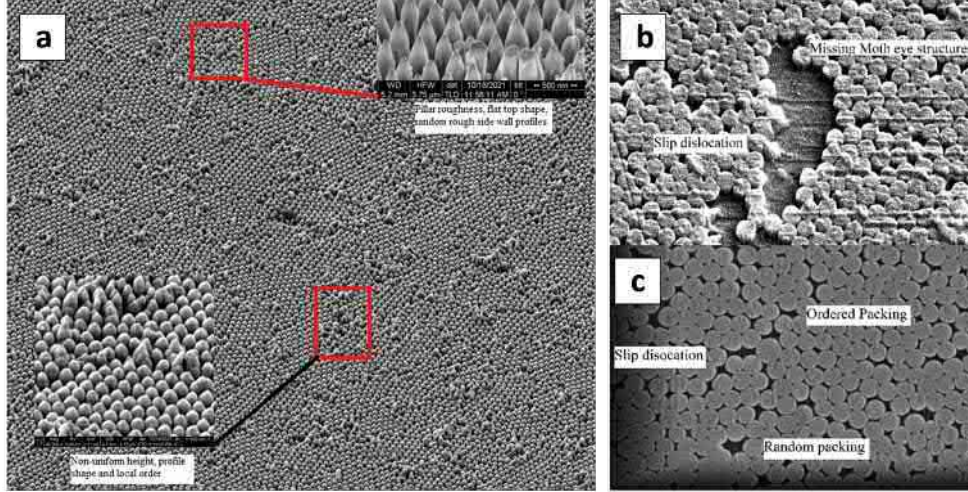


Figure 2.9: SEM of diamond moth-eye surfaces **a)** fabricated for this work, using LB deposition and RIE, with etching related defects to pillar height and profile, including **b)** void defects from Belcourt *et al.* [23] **c)** and packing related order defects observed after deposition and etching of nanosphere monolayers [23].

While self-assembled films produce ordered microstructures, they frequently exhibit a variety of defects [31], limiting their use in a variety of industrial applications that require high-quality and precision films. Sphere vacancies, line dislocations, and random position errors affect the optical properties. Line and point imperfections are the most noticeable flaws in colloidal crystal images. Line defects are defined by the fractional displacement of an entire crystal segment, whereas point defects are defined as isolated spherical voids in otherwise perfect monolayers. The regularity of the sphere size will also influence the order and quality of a monolayer. The nanospheres have different sizes, which may not be significant on a local scale, but cumulatively the standard deviation of the diameter causes strains in the lattice at various points, resulting in voids, fissures and irregularities in the monolayer lattice (Figure 2.9b) [35]. As a result, random tessellated disordered patches are frequently observed between two closely packed domains as observed in Figure 2.9c. In addition, when two or more nanospheres meet, the impact forces must be dissipated by either the displacement of the nanospheres onto a higher layer or by creating additional area within the lattice [35]. The actual size of the disorder inside monolayer sites is determined by surface topology analysis and the precision of the lithographic technique used in fabrication.

Numerous investigations have shown that the presence of faults correlates with decreasing reflectivity within the intended operational wavelength of the AR device [3, 38, 32]. However, it was not possible to assess the effect of deficiencies in optical quality consistently in those conditions. Reducing the defects in these two-dimensional monolayers, and consequently, bottom-up fabricated moth-eye surfaces, is a long-standing problem, and several studies of the fundamental physics and techniques for defect reduction have been reported in literature [24].

2.3.2 Studies of defect tolerance and sensitivity

Few studies have been performed that quantify or extensively investigate the influence of fabrication related defects or non-uniformities that occur randomly or systematically [16]. In general, it has been observed that when the surface parameters of the moth-eye were within tolerance ranges, the design of the moth-eye structure and the effective transmission were robust [44]. Therefore, the basic directives for the moth-eye design are:

1. The protuberances must have a graded shape from tip to base.
2. Tips may be flat if the filling factor is very small.
3. The bottom gap space should be small, with relative size compared to the periodicity of less than 15%.

An analysis of variance (ANOVA) approach was used to determine the contribution of individual design parameters to performance [45]. Imada *et al.* and Sabui *et al.* observed theoretically and experimentally that the structure height and periodicity were parameters with strong influence upon the transmission of moth-eye surfaces, with higher sensitivity and lack of tolerance to the variation of either [44, 45]. Moth-eye structures can, however, be manufactured within permissible tolerances and can achieve a transmittance of approximately 99% [44].

2.4 Summary

Nano-structured moth-eye surfaces are one of the anti-reflection technologies outlined in this chapter that are projected to be effective for a wide range of spectra while still having the ability to be mass-produced on a large scale [35]. Therefore, there is interest in low-cost fabrication methods of moth-eye surfaces. Langmuir-Blodgett deposition is an attractive process for creating a uniform and homogeneous textured surface on moth-eye structures due to its affordability and low cost. Additionally, by utilising the Langmuir-Blodgett technique, large areas can be nanostructured with a resolution of less than 100nm and over an area of many square centimetres [34]. To improve the efficiency of diamond-based moth-eye ARS fabrication using nanosphere lithography, it is necessary to evaluate the effect of a variety of defects on the surface's AR properties. However, due to the complexity of the parameters affecting the optical properties, the sensitivity of the moth-eye AR surface design and performance has not been investigated in detail. Thus, it is critical to consider imperfections and defects in moth-eye ARS in general, as well as the types of defects associated with bottom-up-top-down hybrid nanolithographic technologies in particular.

Chapter 3

Simulating moth-eye surfaces

In this chapter, we develop simulation methods to characterise the sensitivity of the transmittance to defects in the moth-eye texture or structure. We set up the model to investigate how optical qualities are correlated with the structural quality of the surface.

The outlined modelling problem focuses specifically on electromagnetic wave propagation in diamond moth-eye surfaces with defects. It must be constructed with knowledge of the simulation domains, geometries, stochastic surface formation of surface topology, material properties, and incident wave behaviour. The FEM technique requires the defining initial and boundary conditions and the structure's geometry, which we will set up in the following sections. We will also show how to set up partial differential equations describing the physics in this specific structure. Finally, we will focus on the modelling of defects that closely resemble the stochastic disorder and systematic fabrication errors or systematic imperfections that occur in manufacturing structures of the moth-eye textured surfaces which affect their interactions with light [46].

3.1 Modelling simulation tools and procedure

3.1.1 Assumptions for the model

The simulation model is constrained to physically correspond to the experimental diamond moth-eye surface under ideal conditions that isolate the surface's optical response. The wave problem of the model under discussion encompasses three assumptions about light that illuminates a shaped-modulated moth-eye surface: a monochromatic plane wave in transverse electric (TE) polarisation, a plane light source with a full-field incident scheme, and a single polarisation of the light source. It is further assumed that plane-wave light has wavelength $850nm$ for all experiments. This wavelength is of particular interest for biological applications in which diamond windows are used to encapsulate electronics [9]. It is assumed to be sufficient to investigate single polarisation of incoming light because the nanostructure surface, like a uniform surface, is polarisation independent due to stochastic equivalence to an unbiased surface direction. External parameters such as applied pressure are assumed to be constant across the substrate and consistent with room temperature.

Maxwell's and Fresnel's equations are used to determine the propagation of light at the incident boundary. The system has several interfaces - between air and diamond moth-eye pillars, between diamond structure and the substrate, and between the substrate and air (when exposed). All of them are part of the modelling scheme. The fundamental assumption is that the surface can be stochastically modelled - boundaries will only describe a particular instance (realisation) of the real surface with defects. Any surface perturbation, in principle, degrades the electromagnetic (EM) wave contrast and wavefront. This identifies three possible modes of degradation for the beam passing through the moth's eye surface: power loss through the surface, diffuse reflections, and development of wavefront

non-uniformity. Because the maximum transmission of incident light through the surface is desired, the transmittance value will serve as the primary indicator of the surface's optical efficiency.

Finally, random or systematic changes in the texture of the moth-eye's surface will represent defects introduced during deposition and etching fabrication processes. Here defects are interpreted as deviations from ideal (reference) patterned structure. When applied to the parameterised moth-eye surface topology, they are spatial and continuous variations of the basis set of parameters used to produce the surface geometry. The fabrication process is assumed to be intrinsically Gaussian in terms of the physical processes that generate defects. This may not always be the case when uncontrolled impurities, such as dirt or contaminants, are introduced during deposition. Such modifications are not considered here. Even in instances in which processes do not satisfy the normal distribution, a sufficiently large sampling of the means of distributed features, regardless of the initial distributions, will yield a Gaussian process. Thus, randomisation is a convenient technique for addressing issues with moth-eye AR surfaces subject to constraints imposed by fabrication methods.

3.1.2 Simulation pipeline

An ideal subwavelength grating is a periodic structure defined by its unit cell and translation vectors (period). Unfortunately, real-world manufactured surfaces will not have perfectly consistent period or unit cells - period and height will vary depending on the manufacturing process. In order to simulate the effect of the subwavelength grating's imperfection on the transmittance of an AR structure, numerical methods were used to investigate both a statistical variation in the height and radius of the AR structure and also a statistical variation in the lateral spacing between single protuberances [38]. The mathematical approach is schematically depicted in Figure 3.1.

To simulate the moth-eye surface under a variety of defect conditions, a three-dimensional model was created in *MATLAB 2021b*. It was then solved on a High-Performance Computing system using *COMSOL Multiphysics 5.6* to find the transmittance of the generated surface. Once a solution was obtained, post-processing was used to generate a table of defect metrics and transmission values extracted from the solution, as shown in the simulation flow chart in Figure 3.1.

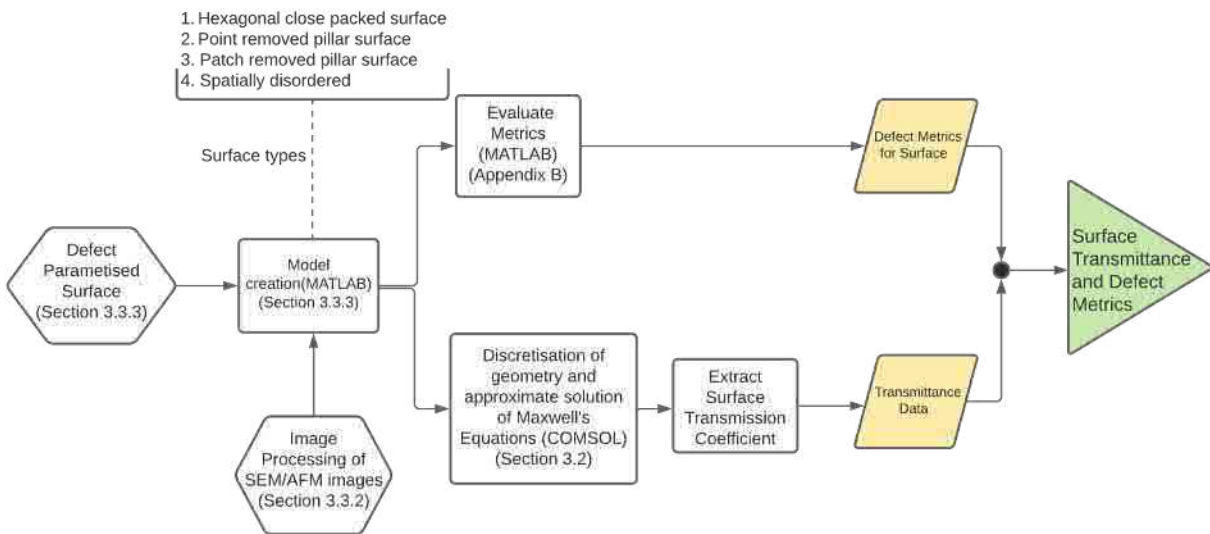


Figure 3.1: Schematic diagram of the simulation method.

3.2 Model description

Numerous wave propagation problems have been statistically solved in the past for the interaction of an incident wavefront with an inhomogeneous or rough surface medium [47], given the condition that the scatterers are sufficiently large in comparison to the incident wavelength or because the scatters can be considered a single particle. However, when there are numerous scatterers with subwavelength local sizes, such as the random surfaces caused by defects considered here, the phases of all contributing scatterers must be considered, complicating the conventional statistical approach. Furthermore, when local surfaces are non-uniform, neither the EMT theory nor the Finite Difference Time Domain approaches are robust enough to handle complicated geometries. As such, *COMSOL Multiphysics* was chosen as the primary simulation tool to perform a first-principles solution to Maxwell's equation for generated moth-eye surfaces.

We chose the frame of reference such that the moth-eye structure occupies the $x - y$ plane, with pillars protruding into the z direction. The incoming wave is perpendicular to the structure with the wavenumber along the z direction and electric and magnetic fields laying in the $x - y$ plane. Maxwell's equations governing spatial distribution of electric and magnetic fields are:

$$\left[\frac{\partial^2}{\partial x^2} + \frac{\partial^2}{\partial y^2} + \frac{\partial^2}{\partial z^2} + n^2(x, y, z)k^2 \right] E_i(x, y, z) = 0 \quad (3.1)$$

$$\left[\frac{\partial}{\partial x} \frac{1}{n^2} \frac{\partial}{\partial x} + \frac{\partial}{\partial y} \frac{1}{n^2} \frac{\partial}{\partial y} + \frac{\partial}{\partial z} \frac{1}{n^2} \frac{\partial}{\partial z} + k^2 \right] B_i(x, y, z) = 0 \quad (3.2)$$

where n is index of refraction that defines the structured layer (diamond pillars, voids, etc.), and $k = 2\pi/\lambda$ is the wave number (in vacuum). For incoming electromagnetic field components, $E_i^{(in)}$ and $B_i^{(in)}$, the scattering field, $E_i^{(out)}$ and $B_i^{(out)}$, is computed as:

$$E_i^{(out)} = E_i - E_i^{(in)} \quad B_i^{(out)} = B_i - B_i^{(in)} \quad (3.3)$$

where E_i and B_i are total electric and magnetic field components. The above equations are discretised using the adaptive FEM scheme (see Appendix A). The diamond surface and air had maximum mesh sizes set to eight mesh elements per wavelength, with finer meshing applied adaptively. This allows addressing features of very different length scales (grating columns vs distortion on their surface) while keeping the total number of mesh points reasonable. Periodic boundary conditions in the x and y directions are not necessary but were used in some cases. At the z -axis boundaries, a perfectly matched layer condition was imposed. The incident medium (above the structure) was assumed to be a vacuum, and the substrate was set as a dielectric medium with or without losses. In the simplest base case, the structure was set (via n) as an axially symmetric ellipsoidal pillar-like array, shown in Figure 3.2, as occurs in the natural moth's eye structure [48]. In this case, for a circularly symmetric structure in a hexagonal packing arrangement at normal incidence, investigation of a single P polarisation of the incoming light is sufficient [49].

Transmittance T is then obtained by $T = 1 - R$, assuming no losses ($A = 0$). The latter has been verified by simulation – diamond has a negligible specular absorption in the near-infrared – and is consistent with experiments [50].

3.2.1 COMSOL specification of the close-packed moth-eye surface

The ideal moth-eye surface design is based on the repeated hexagonal pattern of a semi-ellipsoidal pillar on a closed packed surface as shown in Figure 3.2. For an ideal AR surface, the pillars are located at the lattice points of a hexagonal closed packed array. A single moth-eye structure is the fundamental unit of the *COMSOL* theoretical model. A three-dimensional cuboid is established as a unit superlattice, as shown in Figure 3.2. The moth-eye unit cell is parametrised by height, h (nm), period (x,y), p_x, p_y (nm) and radius, r (nm). The isotropic material of the pillars and substrate is defined as diamond in *COMSOL* with refractive index calculated by the Sellmeier equation for synthetic diamond:

$$n^2(\lambda) = 1 + \frac{A\lambda^2}{\lambda^2 - B}. \quad (3.4)$$

where λ is the wavelength in the medium, and $A = 4.658$ and $B = 112.5 \cdot 10^{-9} \text{ nm}^2$ are parameters obtained in reference [51] for isotropic synthetic diamond surface.

The substrate thickness is set to $\lambda/2n_{\text{diamond}}$ which ensures that evanescent waves in the modelling domain vanish.

Table 3.1: The four geometrical parameters used in the simulation

Parameter	Symbol	Expression
Base radius (nm)	r	-
Pillar height (nm)	h	-
Periodicity in x direction (nm)	p_x	$p_x = 2r$
Periodicity in y direction (nm)	p_y	$p_y = \sqrt{3}p_x$

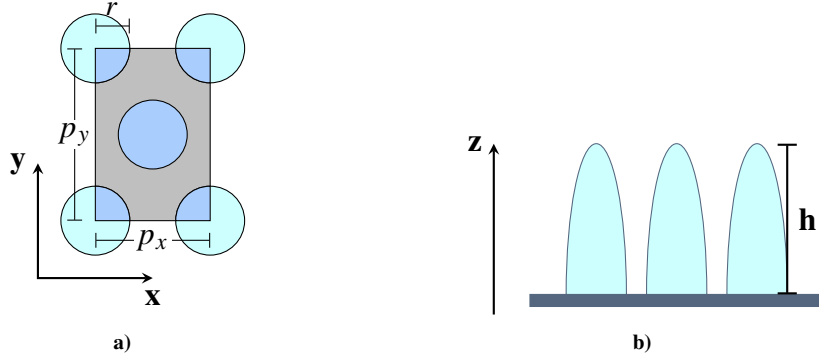


Figure 3.2: **a)** Top view of the COMSOL moth-eye unit cell, **b)** profile view of moth-eye unit cell

The ideal shape profile is defined by Equation 3.5,

$$z_0(x, y) = h \left[1 - \left(\frac{x}{r/2} \right)^2 - \left(\frac{y}{r/2} \right)^2 \right]^{1/2} \quad (3.5)$$

where x and y are the axes parallel to the surface, z is the height perpendicular to the surface, h is the element height, and r is the base width.

3.2.2 Geometry and boundary conditions

Appropriate boundary conditions must be used to approximate the correct electromagnetic wave behaviour within the simulation domain and determine the reflection and transmittance coefficients through the FEM solution of Maxwell's equations. The simulation domain is divided into regions where the incident monochromatic wave is projected into the diamond substrate or reflected away from the surface. Due to the aperiodic nature of the defects and the computational tractability of the simulation domain, the moth-eye surfaces investigated in this project require the simulation of both infinite periodic and finite surfaces. Periodic boundary conditions apply to simulations in which the topology of the moth-eye is uniform and they become prohibitively challenging to solve as domain sizes and mesh elements increase. Where the appearance of defects disrupts the global symmetry of the moth-eye surface, finite boundary conditions are used. Additionally, the number of mesh elements is significantly less than the number required for periodic boundaries.

Using 3λ for the height of the air domain improves the resolution of the reflected wave at the boundary conditions (port and PML). A parametric study was conducted over a range of air domain heights to determine the optimal domain height and revealed that the solution converged to a constant value above 3λ . Furthermore, a domain height of 3λ was found to be the smallest possible computational domain to arrange *COMSOL* input source and boundary ports above and below to avoid parasitic reflections (and interference) coming from the port (boundary) above the source.

The incident light is loaded by port near the upper surfaces of the model and onto the XOY plane along the angle $\theta = 0^\circ$ with the z -direction as shown in Figure 3.3. The moth-eye structure conforms to the Floquet periodic condition, and the wave vector for the Floquet periodicity is calculated by periodic reference ports.

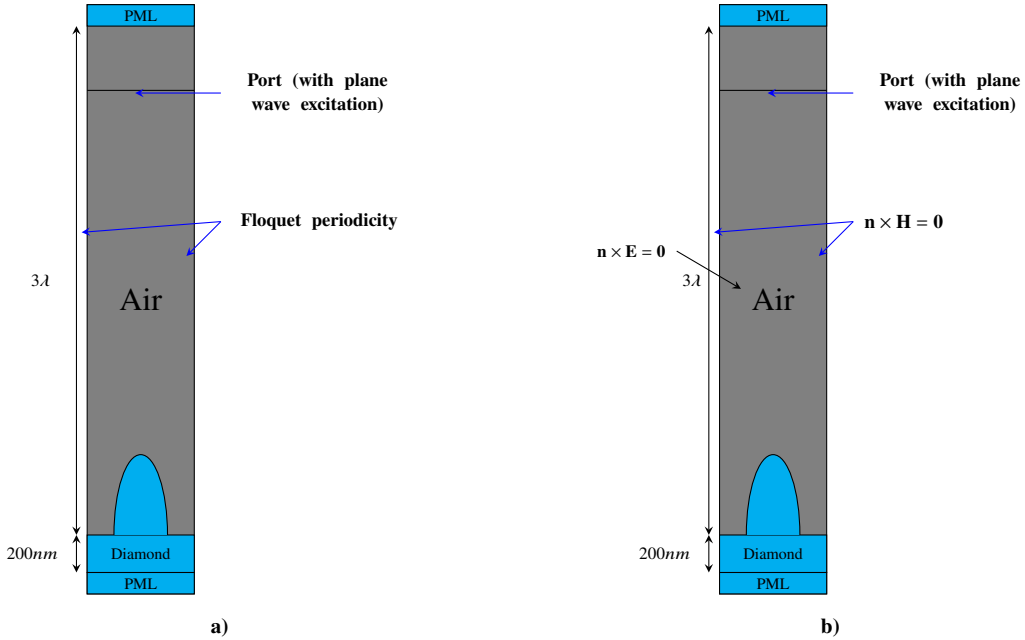


Figure 3.3: COMSOL computational region with air domain height equal to 3λ and diamond substrate thickness equal to $200nm$ shown with **a)** periodic boundaries and **b)** finite boundaries, height. The incident light is loaded by the port boundary at the upper surfaces of the model and incident normally on the simulation surface

Applicability of boundary conditions and effects on solution validity

The simulation model is developed with simplified boundary conditions when random deviations are applied to the surface. Due to environmental factors such as differences in the incident wave medium other than air, non-normal incidence angles, incident light polarisation, and multiple wavelengths, the generality of boundaries cannot be guaranteed. Furthermore, random variations in the surface topology introduce additional reflection from the boundaries and the possibility of grazing or absorption. In order to avoid these problems, the modelling is limited to the simpler case of monochromatic light, incident normally on a diamond medium.

A framework assuming the behaviour of the surface when it interacts with incident light is applied in accordance with the relative scale of the varied surface parameter and complexity of the model. Two scenarios for boundary conditions are developed for the range of geometries to be considered as either local or global features of the simulated surface, namely: (1) local morphological variation and (2) global topological variation. Thus, periodic boundaries simulate domains with a single unit cell, whereas finite boundaries simulate extended simulation surfaces with a non-uniform topology.

Perfect Matched Layer (PML)

At the top and bottom of the simulation domain, PMLs serve as absorbing boundaries for the reflected and transmitted waves. By absorbing the excited mode from the source port and any higher-order modes generated by the surface, the PML prevents waves of any frequency, polarisation, or amplitude from reflecting into the simulation domain from the boundary. In this way, the PML allows for the scattering process to be accounted for as the incident wave will be absorbed and not included in the reflectance or transmittance [52]. Port boundary conditions are located next to the PMLs, and adjacent to the air domain and substrate. The port boundary conditions automatically determine the reflection and transmission characteristics by evaluating the incident wave power. Because Maxwell's equations are implemented in their frequency-dependent form, the thickness of the PML layer is independent of the wavelength [53]. Additionally, because real diamond substrates can be close to 1mm thick, the modelled substrate medium is approximated as semi-infinite by including a PML boundary beneath the substrate in the model.

Periodic boundary conditions

In order to investigate the transmittance behaviour of the moth-eye surface when the geometry of the moth-eye is uniform across all pillars on the surface, a periodic unit cell composed of a single pillar is chosen, as illustrated in Figure 3.3a. The infinite two-dimensional array of pillar bases is simulated using Floquet-periodic boundary conditions on four of the unit cell's sides and periodic port conditions at the incident wave's input and output.

Finite boundary conditions

Defects introduced in uniform moth-eye structure lead to asymmetry and randomness, breaking the translation symmetry of the ideal surface Figure 3.3b. Consequently, periodic boundary conditions are no longer applicable as they produce non-physical effects at the boundary of the simulation domain. Instead, the finite boundary conditions, equivalent to a "no-flux" condition, are applied at the side

boundaries of the simulation domain. Generally, the periodic port is not used for geometries with irregular boundaries. Thus, the sidewall boundaries are set to either perfect magnetic conducting (PMC) or perfect electric conducting (PEC), see Figure 3.3.

Simulation validation

The accuracy of the *COMSOL* simulation is validated using analytical calculation of the transmittance for an optically flat diamond surface and two processed samples [23]. The simulation results agreed with the theoretical results from the Fresnel equations and with small residual to the transmittance measurements for the two moth-eye surfaces. Two simulated surfaces were tested for each sample: (1) a unit cell with periodic boundaries and (2) a finite domain with moth-eye pillar locations inputted from an SEM image of the surface. The transmittance values are expectedly similar due to the high packing of the surface - the finite domain is comparable to the unit cell. Overall, the fabricated moth-eye pillars demonstrated good conformity with the predicted values from the simulations and, in turn, supported the validity of the developed *COMOSL* model.

Table 3.2: Transmission coefficient results obtained on 3 samples using unit cell and extended surface simulation.

	Experimental value	Unit cell simulation (1x1 area)	SEM imaged surface simulation
Untextured CVD diamond	0.830 (Theoretical)	0.830 ± 0.001	0.830 ± 0.001
Polycrystalline diamond moth-eye surface (hemispherical structures of base radius equal to (150nm))	0.965 ± 0.009	0.972 ± 0.001	0.950 ± 0.001
Single crystal diamond moth-eye surface (pillar structures of height equal to 600nm and base radius, 150nm)	0.995 ± 0.003	0.995 ± 0.001	0.990 ± 0.001

3.3 Defect generation

3.3.1 MATLAB defect simulation approach

As discussed in Chapter 2, random and systematic defects require a probabilistic approach to the simulation of the moth-eye textured surface. An appropriate set of parameters is specified to accurately address defect features of a real moth-eye surface. Defects are uncontrolled discontinuities or irregularities of a chosen basis set of continuous parameters used to model the geometry of a surface. Using the *COMSOL* Livelink for *MATLAB* interface, a custom *MATLAB* function drives the generation of *COMSOL* models. Specifically, the custom function passes a vector of parameters that control the geometry of the *COMSOL* moth-eye surface model. Custom image processing scripts for SEM and AFM data were used to identify deviations introduced to the ideal moth-eye surface texture during fabrication. The statistically distributed topological defect features: deviation in height, radius, distribution of pillar spacings, short- and long-range order, and vacancies are measured using a set of defect metrics that quantify the deviation from an ideal moth-eye surface caused by defects. In the context of uncertainty quantification studies of Mahmoud *et al.* [46], the simulation design implemented in this work models the errors in fabrication as random noise applied to the topology parameters of the moth-eye surface (as described earlier in this Chapter).

3.3.2 Inclusion of SEM and AFM data in defect generation

For the theoretical analysis and modelling of moth-eye surfaces structures, the physical parameters of the structures such as the pillar radius r , radius deviation σ_r , height deviation σ_h and defect parameters are determined from experimentally realised surface texture. This subsection describes the image analysis performed on the SEM images for extracting the desired parameters. These will serve as input in the modelling of the defects.

The moth-eye surface's radii and other spatial features are extracted from SEM images by a custom statistical image analysis script written using *MATLAB* libraries. Standard particle detection methods, image binarisation and segmentation, are used to detect the location and radii of moth-eye pillars from top-down SEM images as presented in Figure 3.4. The empty area between pillars and in untextured regions are also quantified. These methods are commonly used for the spatial analysis of colloidal monolayers [54]. The script produces a table of detected pillar locations and statistics for the distribution of the textured and untextured areas on the fabricated moth-eye surface.

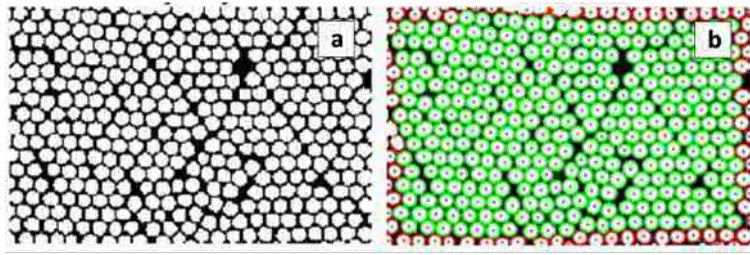


Figure 3.4: **a)** Original SEM image and **b)** image obtained after applying standard particle detection method from *MATLAB* Computer Vision Toolbox and OpenCV interface.

3.3.3 Defect parameters and surface generation

Morphological localised defects

Depending on the fabrication conditions, the local morphology of the moth-eye pillar may deviate from that of the ideal semi-ellipsoid structure. Therefore, two profile variations are simulated here; flat-topped Gaussian and randomly roughened pillars. The flat-topped Gaussian has appeared in other works that have investigated the influence of deviations in the designed surface geometry on the properties of an AR surface [38].

Flat-top Gaussian

In the case of non-smoothly tapered moth-eye structures caused by an etching defect, as illustrated in Figure 3.5a, a flat-topped Gaussian or super-Gaussian profile is an appropriate model. The super-Gaussian shape, Equation (3.6), is parameterised using an eccentricity factor Ω that flattens the curvature of the tip. It approximates real structures that are incorrectly etched (Figure 3.5b).

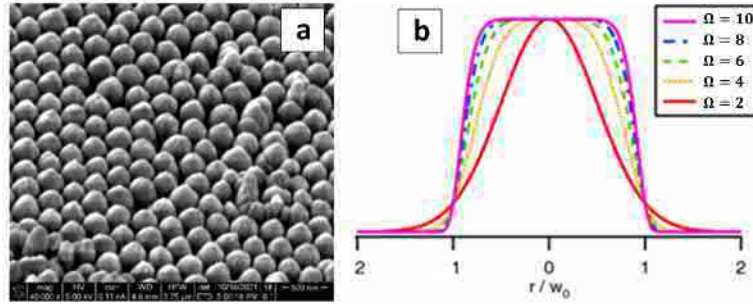


Figure 3.5: **a)** SEM of diamond moth-eye surface fabricated in this work **b)** Cross-section of supergaussian profile for Ω from two to ten.

$$z(x, y) \propto e^{-[2\rho(x^2+y^2)]^\Omega} \quad w_0 = 2\sqrt{2 \ln 2} \rho \quad (3.6)$$

Randomly roughened profile

The roughened sidewall profile of pillars is constructed by introducing small-scale local deviations from the shape of a geometrically ideal structure. Random deformation is applied to the semi-ellipsoid shape by a stochastic noise function. The function, Equation 3.7, is parameterized by the spatial frequency resolution $N(nm^{-1})$, spectral exponent b , and amplitude sq . The variables control the parametric surface of the randomly roughened pillar. The root mean square roughness (RMS) is evaluated as the standard deviation of the roughened moth-eye pillar from the ideal shape, z_0 , or the error in the surface according to Equation 3.8, where L is evaluated over the size of the pillar.

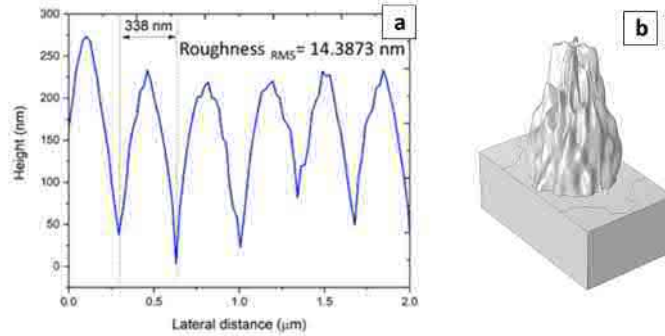


Figure 3.6: **a)** Height profile of diamond moth-eye pillars measured using AFM **b)** COMSOL model of unit cell moth-eye randomly roughened pillar for $N = 15nm^{-1}$, $sq = 0.15$, $b = 1.25$ and $RMS = 25nm$

$$z(x, y) = \sum_{m=-M}^M \sum_{n=-N}^N a(m, n, sq) \cos(2\pi b(mx + ny) + \phi(m, n)) \quad (3.7)$$

$$RMS^2 = \frac{1}{L^2} \int_0^L \int_0^L \left((z(x, y) - z_0(x, y))^2 \right) dx dy \quad (3.8)$$

Height and Radius deviations of moth-eye pillars

To quantify local deviations of the moth-eye pillars from one another, the distribution in height and radius are found using SEM and AFM. A Gaussian fit for the height etched profiles was found using the software *WSxM* [55]. The custom image processing in *MATLAB* was used to determine the distribution of pillar radii. An example analysis is presented in Figure 3.7 where it is seen that the height of the moth-eye pillars is distributed normally, and the radii are distributed with skewed function. In practice, the distribution will vary according to the etching parameters [56]. The deviation of moth-eye pillar heights and radii are modelled using Gaussian and half Gaussian distributions:

$$p(h) = \frac{1}{\sigma_h \sqrt{2\pi}} \exp\left(-\frac{(h - \bar{h})^2}{2\sigma_h^2}\right) \quad p(r) = \frac{1}{2\sigma_r \sqrt{2\pi}} \exp\left(-\frac{(r - \bar{r})^2}{2\sigma_r^2}\right) r_0 \geq r \quad (3.9)$$

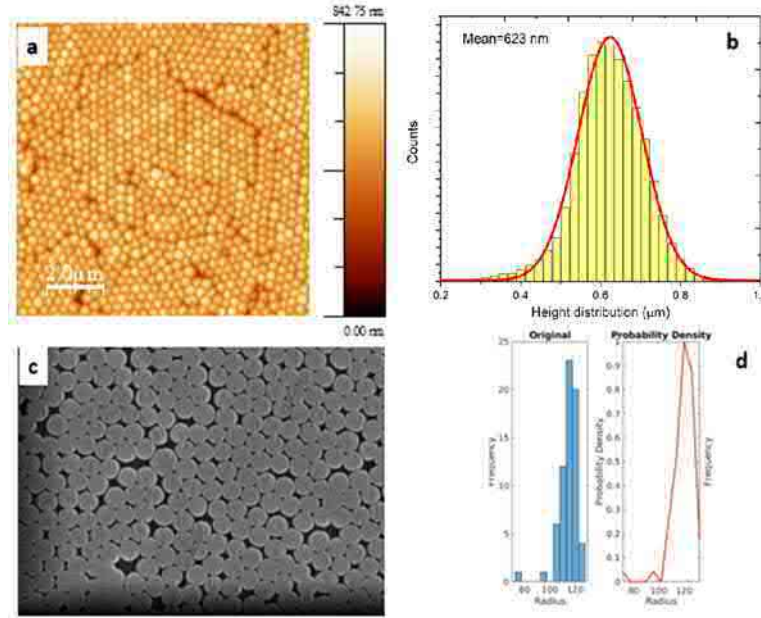


Figure 3.7: **a)** AFM of diamond moth-eye surface from Belcourt *et al* [23] **b)** Histogram of moth-eye pillar height with $\bar{h} = 623\text{nm}$ and standard deviation of $\sigma_h = 125\text{nm}$ **c)** SEM of diamond moth-eye surface from Belcourt *et al* [23] **d)** Histogram of detected radii and estimated distribution

Packing density and order defects

The defect surfaces presented in Section 2.3 consist of disordered domains and voids or varying sizes. The voids have an irregular appearance and do not relate to the grain orientation. Thus, to simulate such structures, the effects of the deviations must be controllable. The parameter chosen to quantify the packing and related defects is the removal fraction, C . It measures the ratio of the number of moth-eye pillars in the domain relative to the quantity for an ideal hexagonal packed domain. Three algorithms to simulate the appearance of local clustering and missing pillars are implemented: (1) Point defects from a single missing pillar, (2) Local clusters removed as patch defects (3) Nucleation and cluster formation. The first two algorithms are implemented on a fixed hexagonal lattice.

A custom script in *MATLAB* implements each algorithm as a 2D spatial process to assign coordinates for each moth-eye pillar in the simulation domain. For point defects, a Bernoulli trial is implemented

for the number of pillars calculated from C for each moth-eye pillar site in the simulation domain. For patch defects, the Perlin texture algorithm was used to produce randomly appearing patches of random size [57]. To achieve this, it utilises a smoothly varying pseudorandom gradient evaluated throughout the simulation domain with magnitude -1 to 1. By determining a threshold from the removal fraction, C , regions identified below the threshold can be excluded from the simulation domain. This results in randomly appearing patches that have no obvious repeating pattern. Additionally, the Perlin algorithm is chosen as it has a spatial frequency that is invariant under translation. An example is presented in Figure 3.8. It shows a comparison between SEM images of moth-eye surfaces with patch defects and generated Perlin texture domains of the same size.

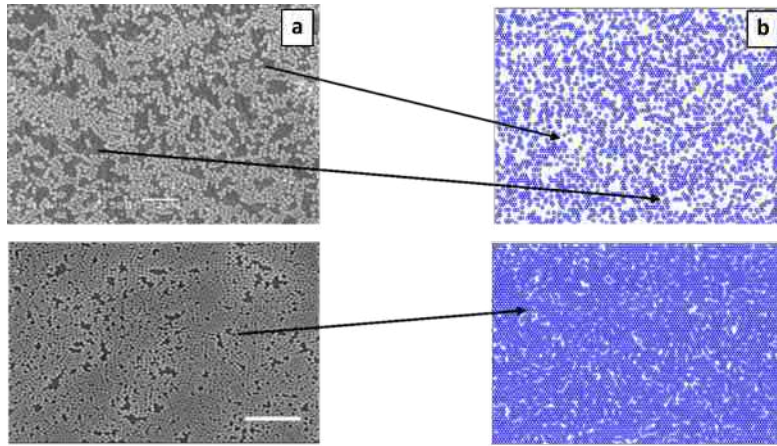


Figure 3.8: The similarity between **a)** SEM of self-assembled silica colloidal monolayers and **b)** Perlin generated texture of randomly appearing patches for the same value of removal fraction, C , ($C \approx 0.45$ (top), $C \approx 0.25$ (bottom)) is presented for two silica monolayer samples from Belcourt *et al.* [23]

Lastly, a molecular dynamics simulation was conducted to simulate the aggregation and clustering observed in colloidal monolayer masks. It modelled nano-sphere self-assembly into a lattice prior to being etched and during deposition. The rationale for this modelling is given by the assumption that the colloids arrange in such a way to minimise the free surface energy in the crystalline phase. The strength of the Van der Waals potential used in the molecular dynamics simulation is approximated by matching the power spectral density of the final simulation state to SEM images of silica nano-sphere deposited using the Langmuir-Blodgett technique.

Defect surface generation

Table 3.3 summarises the defect parametrization. The morphological parameters determining the shape of the local moth-eye profile are distinguished from the global defect parameters affecting the topology of the moth-eye surface. Each parameter is passed as an argument to the *MATLAB* function that creates the *COMSOL* models. Additionally, the random removal process was implemented using the three methods described in Section 3.3.3: point removal, patch removal, or random clustering. The relative intensity of defects can be varied depending on the size of the defect feature's deviation. This enables the effect of increasing defects on the optical properties of the moth-eye surface to be investigated independently or simultaneously. The location and shape distribution data processed from SEM and AFM images may be passed directly into the custom *MATLAB* function. The resulting *MATLAB* function controlling the generation of the moth-eye surface drives both deterministic and

probabilistic generation of simulation geometries, solved in *COMSOL*, to determine the sensitivity of the transmittance to defects.

Table 3.3: Summary of the defect parameters

Parameter	Symbol	Expression
Omega	Ω	-
Spatial frequency resolution	N	-
Spectral exponent	b	-
Roughness amplitude	sq	-
Mean height	μ_h	$\mu_h = \frac{\sum h_i}{(n-1)}$
Mean radius	μ_r	$\mu_r = \frac{\sum r_i}{(n-1)}$
Standard deviation in height (nm)	σ_h	$\sigma_h = \sqrt{\frac{\sum (h_i - \mu_h)^2}{(n-1)}}$
Standard deviation in radius (nm)	σ_r	$\sigma_r = \sqrt{\frac{\sum (r_i - \mu_r)^2}{(n-1)}}$
Fraction of removed moth-eye structures	C	$C = \frac{\# \text{ Removed Structures}}{\# \text{ Total Structures}}$

It is reasonable to expect that the visual similarity of modelled and real distributions will be more increasingly more precise with the increase of the number of generated random values. Morphological variations to the moth-eye pillar are simulated using periodic boundary conditions, and finite boundaries are used for topological defects. To limit model complexity, the defects simulated here are formed as deviations to a perfectly optimised moth-eye surface. Additionally, because simulation inputs are drawn from experimentally large areas, the statistically significant effects of defects on the surface may be evaluated.

Simulation domain size considerations and computational limitations

Edge effects caused by the incident electromagnetic wave source's spot size are not considered. The simulation domain solved for the defected moth-eye surface is $5\mu m \times 5\mu m$, a factor of ten larger than the wavelength used ($850nm$). This was the maximum domain size for which the transmission measurement converged in a reasonable time. The number of Monte Carlo simulations required to generate a sizable data set for further analysis was also a constraint on the simulation domain size chosen in consideration of the total simulation time and available computational resources.

3.3.4 Fabrication and characterisation of diamond moth-eye surfaces

In the present work, in addition to the sample provided from the work of Belcourt *et al.*, two diamond moth-eye surfaces are fabricated following the method reported by the same author [23]. In order to create large-area diamond moth-eye surfaces, a Langmuir-Blodgett film is used to deposit a sacrificial mask of silica nano-spheres onto a single crystal diamond (SCD) substrate followed by reactive ion etching to create the moth-eye texture. At first, a template is created on the $2mm \times 2mm$ SCD substrate using $10mg/mL$ aminated monodisperse silica nano-spheres in ethanol (*Nano Composix Inc.*) with a diameter of $300nm$ (*CVD diamond windows, Diamond Materials GmbH*). This silica-ethanol (S-E) solution is treated with $10mg/mL$ stearic acid (SA) at a volume ratio of 200 : 1. Then, a Langmuir-

Blodgett trough is used to transfer 500 L of the S-E-SA solution onto the hydrogen-terminated diamond surface (*model 711D, 76 cm x 10 m, Nima Technologies Ltd. with a single barrier*). After deposition, the diamond substrate coated with silica is etched using RIE (*PLASMALAB100 ICP380, Oxford Instruments Ltd*). Cyclic diamond-etch/silicon-etch steps with an Ar and CHF_3 gas mixture at flow rates of 15 and 10 *sccm* are used to etch the silica nano-spheres. Furthermore, the diamond substrate is etched by adjusting the O_2 flow rate at 30 *sccm*, and RF and ICP power 20W and 600W, respectively. Seven silica-diamond etching cycle repetitions were used, and the etching phase time for silica and diamond is 60s and 120s, respectively. The chamber was evacuated and purged with nitrogen after completing each phase.

SEM, AFM measurements

SEM measurements were performed using a *Hitachi TM3030* SEM with a 10nm Au coating. AFM was also performed in contact mode with an *Asylum Research Cypher* system. The SEM and AFM images were quantitatively analysed using *MATLAB*, and *WSxM*.

3.4 Gaussian Process Regression

The Model

The Gaussian Process Regression (GPR) model—a Machine Learning algorithm—was used to estimate the transmittance of the moth-eye surface texture based on large amount of training data from numerical simulations performed with *COMSOL*. The GPR approach is suitable in our case because it provides a convenient way to fit data described by an underlying probabilistic processes [58]. There are intrinsic non-linearities present in the defect parameters (Appendix B), which have been defined in this study to measure the moth-eye surface topology related to fabrication uncertainty. The GPR approach is a nonlinear, non-parametric regression based on Bayesian method [59, 60] and designed to work with such data, i.e., to interpolate data points scattered in a high-dimensional space. In other fields of optics [60, 61, 62], GPR has been successfully utilized because of its probabilistic interpretation of predicted output, hyper-parametric adaptive acquisition, simple implementation and flexible non-parametric inference.

Data Generation

The parameter space used to train the model is generated using a Monte Carlo sampling method of the defect parameters $C, \mu_h, \mu_r, \sigma_r, \sigma_h$ which are deviations from the ideal shape and surface packing ($r = 150\text{nm}, h = 500\text{nm}, p_x = 315\text{nm}, p_y = 545\text{nm}$) during fabrication. Further details are provided in Section 4.1.1 in the next Chapter.

Performance results

Our objective was to fit a regression model to the defect parameters and metrics derived from the *COMSOL* simulation data in order to estimate a surface's transmittance. The GPR machine learning model is implemented and then trained using *Python*-based libraries. We tested a variety of other regression models in this process, including regression trees, regression SVMs, regression ensemble

techniques, and GPRs. In order to identify the best approach we used a 10-fold cross-validation to compare the techniques. We report only the performance of the GPR with various kernels using mean absolute error (MAE) and root of mean square error (RMSE) as metrics presented in Appendix C. Our findings demonstrate that the GPR outperforms the above mentioned alternative techniques.

Modelling constraints

An unavoidable obstacle using GPR machine learning for optical meta-surfaces is the amount of time it takes to process (learn from) the simulation data, taking into account that *COMSOL* simulations take significant amount of time as well. The *COMSOL* model mesh size, simulation domain size and complexity—all have an effect on the accuracy necessary to obtain satisfactory results for transmittance and, thus, can not be sacrificed to speed up the process. Yet, the GPR approach still provides the best way to solve this given problem with high precision and accuracy.

3.5 Summary

In this Chapter, we described methods to simulate the role of defects on the transmission spectra of a moth-eye structure. A *COMSOL* and *MATLAB* based simulation approach was developed to determine the transmittance of surfaces with defects motivated from analysis of SEM and AFM images of experimental surfaces. In addition, we have presented the simulation criteria and the boundary conditions as necessary. Numerical results describing the role of defects will be shown in Chapter 4.

Chapter 4

Effect of defects on the simulated transmission of moth-eye structures

This chapter will present a detailed examination of defects based on methods and models explained in Chapter 3. Diamond moth-eye AR defected surfaces were numerically solved using statistical models of defects. FEM is used to quantify the effect of imperfections on effective transmission. We first investigate the transmission efficiency in relation to the surface's regular texture parameters (height, radius, and periodicity) to identify an appropriate ideal geometry for use as the basis for the defect investigation. Defects are classified based on their local and global deviations from the ideal AR texture of the moth-eye surface. Then, local deviations of the moth-eye structure are introduced to account for fabrication-related defects. This is accomplished by decreasing the curvature and increasing the tip width of the ideal structure and further by adding a randomly roughened sub-wavelength profile. Correlations for the effect of spatial disorder on the ideal hexagonally densely packed AR surfaces of moth-eyes are then analysed using the parameters defined in Section 3.3.3. Finally, the overall sensitivity of the diamond moth-eye surface to transmission is deduced from the parametric analysis of the defect-free and defect models studied.

4.1 Parameter space search for the ideal surface geometry

We use FEM simulations to obtain variations of the shape and topological parameters of the moth-eye surface within the unit cell. Figure 4.1 shows the hexagonal unit cell determined by FEM. The structure is defined by four geometrical parameters: radius r , height h , x-period p_x , and y-period p_y . The incident plane wave is perpendicular to the plane of the structures, i.e. $\theta = 0^\circ$ and the refractive index n of the substrate is 2.39 for the wavelength $\lambda = 850nm$. The transmittance for the fixed wavelength of $850nm$ at normal incidence is simulated over a range of periods (p_x and p_y), radii r and pillar heights h .

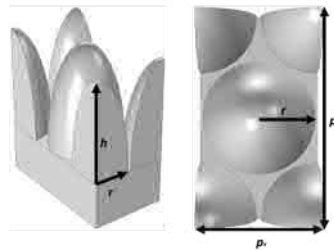


Figure 4.1: Hexagonal closed packed unit cell determined by Finite Element Method (FEM). Here parameters h , r , p_x , and p_y represent pillar height, pillar radius, x-period and y-period, in nanometers, respectively.

Figure 4.2 shows a surface and corresponding heatmap plot, exploring the geometry parameter space over a range of sizes for the close-packed moth-eye unit cell. Three regions of maxima appear, with a transmittance greater than 0.99 in three different domains of height and radius parameter space, under

the assumption of ideal periodicity. This tells us that the transmittance may be optimised with more than one moth-eye pillar shape. Of the two minima which appear in the plot, the one that aligns with two maxima at the height of 700nm is the most interesting. Continuing along the height of 700nm , the transmittance reaches above 99% at the maxima and then falls to 92% as the radius varies from 200nm to 300nm . As the respective change in the diameter becomes close to a quarter-wavelength of the incident light, destructive interference effects become significant.

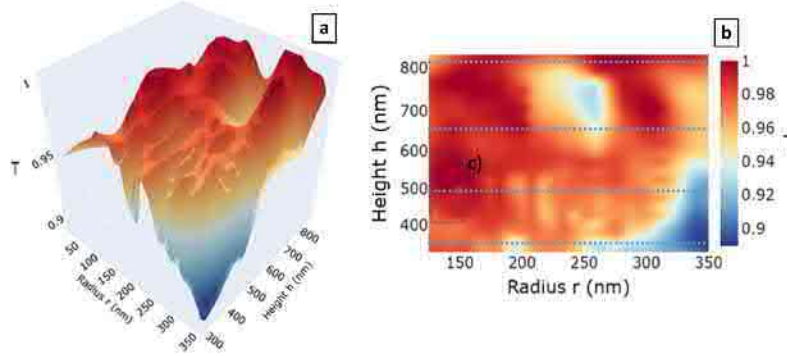


Figure 4.2: **a)** Height, h , and radius, r , dependence of transmittance, T , for moth-eye structure unit cell for close packed case, x-periodicity, $p_x = 2r$, y-periodicity, $p_y = \sqrt{3}p_x$, $\lambda = 850\text{nm}$. **b)** Transmittance as a function of radius, varying from 150nm to 350nm , and height, varying from 350nm to 850nm , for a hexagonal closed-packed unit cell. Dotted lines correspond to curves plotted in Figure 4.3 for cross-sections of transmittance versus radius **c)** Region identified for sensitivity analysis for optimized moth-eye pillar geometry, Section 4.1.1.

The transmission versus radius for different moth-eye structure heights, h , is presented in Figure 4.3. The hexagonal closed-packed lattice structure is maintained over the entire range of the radius values. Reflection is suppressed at 850nm as this wavelength is larger than the critical wavelength, for which the subwavelength condition applies. The critical wavelength, $\lambda_{critical}$ for effective medium spacing is $\lambda/n = 850\text{nm}/2.39 = 355\text{nm}$. The series of plots of transmittance versus radius for a range of moth-eye structure heights, from 350nm to 950nm , are in accordance with the results presented in Figure 4.2 The observed variation in the shape of the moth-eye pillar for each height is due to the interaction of the wavelength with the depth of the surface to produce resonances in the transmittance. The finding appears consistent with the analysis of Boden *et al.* who emphasise the tuneability of moth-eye surfaces for optimal transmission [16].

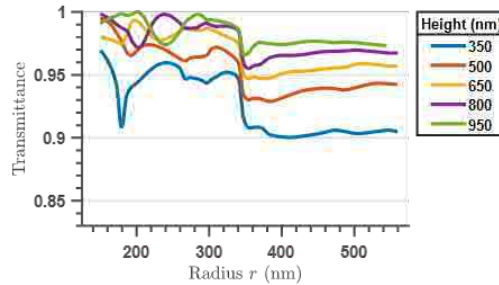


Figure 4.3: Dependence of transmittance on radius for fixed heights of moth-eye structures from 350nm to 950nm for the moth-eye structure unit cell for close packed case.

Since the lateral size of the moth-eye structure must be significantly smaller than the wavelength for it to function as an AR surface, some physical implementations are limited in terms of the aspect ratio of the pillars that can be achieved. Thus it is useful to observe how the sensitivity of the transmittance varies for different aspect ratios.

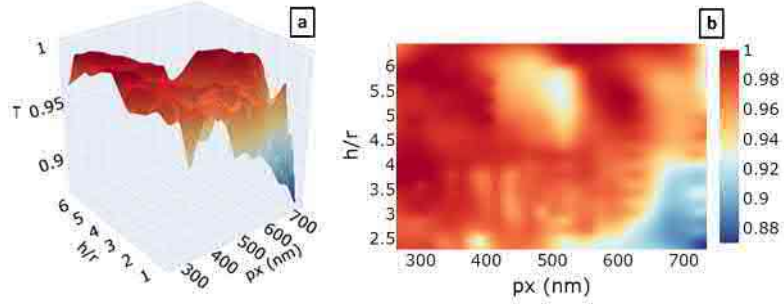


Figure 4.4: Moth-eye surface transmittance plotted against aspect ratio, h/r and x -periodicity, p_x , for hexagonal closed packed unit cell. The plots produced show results similar to those of Sai *et al.* [63]

The transmittance of the moth-eye structure is plotted against the aspect ratio, h/r in the unit cell model in Figure 4.4. The lattice packing is still hexagonal close-packed, so we take $r = 0.5p_x$, without loss of generality. The transmission increases with increasing height and decreasing periodicity or, equivalently, the higher spatial frequency of the moth-eye structures, indicating that the incident wave's path length is longer, implying greater light trapping as predicted in Chapter 2.2. Similarly, as the period and aspect ratio of the moth-eye structure are reduced, the transmittance generally decreases but remains greater than 96%. In general, increased structure density in the air-diamond medium (e.g., smaller periodicity) increases transmission.

4.1.1 Discussion: Transmittance near region of ideal pillar geometry

The parameter space search presented above aims to determine a region of maximal transmittance as a function of parameters that control the moth-eye surface geometry. As shown in Figures 4.1 and 4.3, when the structure radius is reduced to less than $350nm$, transmittance increases rapidly at all pillar heights, with a greater effect at lower pillar heights. Transmission efficiency decreases when feature heights diminishes below about half the wavelength, as illustrated in Figure 4.2. While the variability in the geometry of AR surfaces with moth-eye pillars is broad, there are local maxima and minima in the transmittance of such surfaces, which can be tuned by varying the array's period (Figure 4.4) [16]. When the sidewall slopes' depth and steepness are varied, much more sensitivity is observed. Transmittance values greater than 99% can be achieved in this case. Note, however that optimisation along this route may require extremely large depths. Increasing the height increases the transmittance for all periods, but at the expense of difficulties in experimentally realising features with a high aspect ratio [16]. This is evident in Figure 4.3 where the green curve for moth-eye structure height of $950nm$, is the most robust to variation in radius from r equals $150nm$ to $350nm$. However, structures of this height are a much greater challenge to fabricate [64].

In Figure 4.3, it is demonstrated that the transmittance is relatively insensitive to changes in the radius of the moth-eye structure for values less than $370nm$. This agrees with the range predicted by the condition for the moth-eye surface to behave as an effective medium. For that range, the radius is less than the critical wavelength ($r < 355nm$) and Fresnel reflections are suppressed below the limit of 17%, which is the reflectance for an optically flat diamond with n equal to 2.39 [20].

The performance of a diamond moth-eye structure is nearly insensitive to the pillar height over a radius range of $125nm - 355nm$, with high transmittance values ($> 95\%$) at heights above $400nm$. There

is a gradual increase in transmittance for pillars of varying heights over the entire evaluated radius range (coloured curves). The highest transmittance (99.9%) is achieved in these samples for heights of $500nm$ and $800nm$, while the tallest examined pillar height ($950nm$) transmits light at a rate of 99%, in comparison to the untextured flat diamond surface.

When the critical period is less than $350nm$, the specular light reflection is nearly completely independent of the structure period, as shown in Figure 4.4. Thus we see that structures with larger grating periods, which are easier to produce, do not perform as well. Therefore, the structure's height is the second most important design parameter. As the structure's height increases, the smoothness of the optical transition (from vacuum to substrate) improves, and the amount of reflected light decreases further. Thus, the sensitivity of the transmission to the structure height is highly dependent on the profile geometry chosen.

This analysis demonstrates that the structures act as an effective medium for short periods (e.g. x -periodicity, $p_x < 350nm$), behaving as an impedance matching surface. As predicted by EMT, increasing the height in this region causes a rapid increase of transmittance, without significant deviation except for small amplitude interference fringes appearing like troughs in Figure 4.4, caused by discontinuities at the structure's boundaries. As the period approaches the wavelength, the resonance behaviour becomes more complicated. We observe a region of low reflectance and high transmission at relatively low feature heights between these two regimes. This is ideal for the design of artificial moth-eyes.

Ideal geometry identification

As we saw in the previous section, ideal values for height and radius are a radius of $150nm$ and a height of $500nm$. This radius and resulting close-packed spacing are consistent with effective medium theory, with critical wavelength, $\lambda_{critical} = 355nm$, as the effective medium spacing value. Since $850nm$ is greater than the critical wavelength, a $355nm$ subwavelength condition applies, ensuring that the moth-eye structures function as an impedance matching device. In order to replicate the conditions of fabrication in Belcourt *et al.* [23], limitations are applied according to the heuristics of the fabrication methods. Physical constraints on structure geometries are imposed by the $300nm$ diameter of the mask nanoparticles and the etching depth of the single-crystal diamond surface [23]. Moreover, the choice of height is appropriate given the difficulty of fabrication of large aspect ratio surfaces [15, 16]. The values of $r = 150nm$ and $h = 500nm$ were verified by performing simulations mentioned above for each specific value, optimising the transmittance over 500 iterations using the machine learning Monte-Carlo based gradient descent method package in Uqlab [65]. Thus, the ideal geometry for the subsequent analysis is represented by those values, with pillar density imposed by periodicity according to the close hexagonal packing: $p_x = 315nm$, and $p_y = 545nm$. The mean height and radius used in the remainder of this section are set to this ideal (reference) geometry.

4.1.2 Deviation from the ideal geometry and effect on the transmittance

To examine the sensitivity of the unit cell height to base width ratio of the etched ideal diamond moth-eye surface, we vary radius, height and spatial period. The fabrication limits define a region of interest - changes in the geometry parameters are affected by the selected initial size of the nano-spheres, diameter equal to $300nm$, and degree of deviation of etched moth-eye structure height. The upper

bound for radius and lower bound for periodicity are given by the optimised moth-eye pillar geometry from the previous subsection ($r = 150nm$ and $p_x = 315nm$, respectively).

Figure 4.5 demonstrates that the sensitivity of the transmittance to variation in radius and spacing is greater than the sensitivity to variation in height overall. As shown in Figure 4.5a, when the radius is ideal, the transmittance is significantly less sensitive to variations in height, but not in spacing. Additionally, according to Figure 4.5b, when the radius of the moth-eye pillar is half of the ideal, the sensitivity of the transmittance significantly increases to both spacing and height. In Figure 4.5c, when the height is ideal, it is critical to maintain as close to perfect hexagonal packing as possible without reducing the pillar radius. In particular, for x -periodicity less than $500nm$ the transmittance is noticeably higher than for x -periodicity greater than $500nm$. This conforms to the expectation that interference effects will increase when the pillar separation is greater than half the wavelength, so the sensitivity of the transmittance to variation in the spacing of pillars will be greater. Thus, the transmittance is increased by narrowing the gap between the pillar bases.

The two-dimensional plots in Figure 4.6 further demonstrate qualitatively that the transmittance is sensitive to changes in the shape of the moth-eye structure. It also confirms the transmission's local maximum with the geometry parameters chosen in the preceding section. In Figure 4.6a, the height of the moth-eye pillar has minimal effect on the ideal shape's transmittance. Conversely, the radius is shown to be the parameter with the greatest effect on the transmittance. When the base radius of the moth-eye structure is $50nm$, the surface loses all the efficiency gained by the textured structure and the transmittance approaches that of the untextured diamond surface, i.e. 0.83. As shown in Figure 4.6, varying the period of the pillars has a non-linear effect on the transmittance. As the period increases, the transmission drops from 0.998 to 0.965 when the periodicity reaches half the wavelength. This corresponds to the expected increase in interference effects discussed in Section 2.2.

The above analysis shows that when features are deformed at a constant rate, the transmission is primarily sensitive to radius and periodicity. Furthermore, transmission surfaces, Figure 4.5, and cross-section plots, Figure 4.6, demonstrate that an increase in gap size between moth-eye pillars has the greatest effect on the transmission. As a result, it is evident that reducing the gap between the base of the pillars will further increase transmittance.

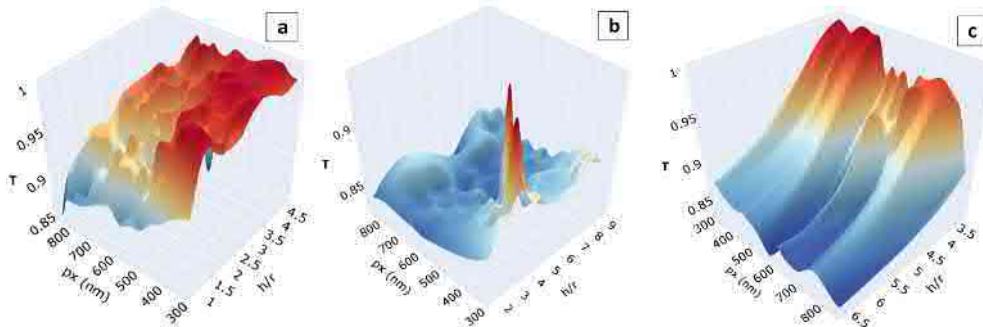


Figure 4.5: Transmission as a function of periodicity and aspect ratio for **a)** a constant radius, r , of $150nm$ to demonstrate the effect of varying periodicity and height on the ideal moth-eye geometry. **b)** A constant radius of $75nm$, illustrating the variation of transmission with height and periodicity for radius much less than the ideal corresponding to spacing defects. **c)** A fixed height of $h = 500nm$, where transmittance decreases with two maxima appearing for half-wavelength periodicity near $p_x = 500nm$. x -periodicity corresponds to dense packing at $p_x = 315nm$ and sparse packing at $p_x = 800nm$.

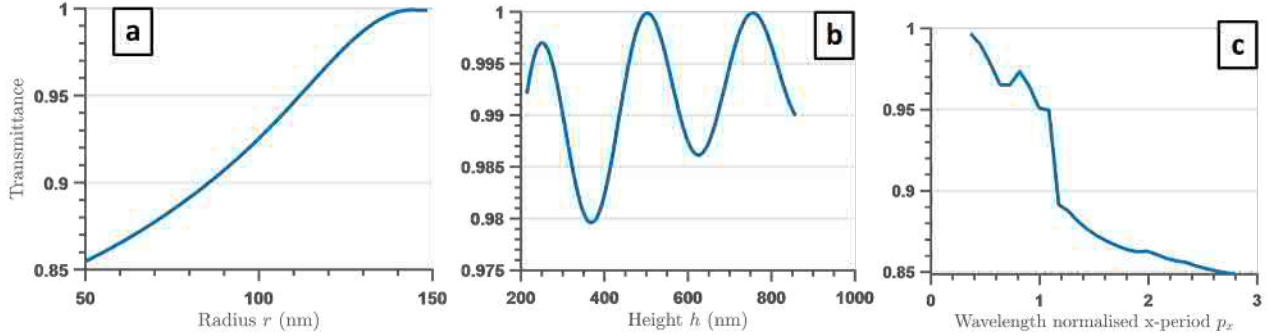


Figure 4.6: Cross sections of Figure 4.5 showing the independent deviations from the ideal optimised parameter values of the unit cell moth-eye geometry parameters for fixed **a)** $p_x = 315\text{nm}$, $p_y = 545\text{nm}$, $r = 150\text{nm}$ **b)** $p_x = 315\text{nm}$, $p_y = 545\text{nm}$, $h = 500\text{nm}$, **c)** $h = 50\text{nm}$, $r = 150\text{nm}$

4.2 Transmission sensitivity to simulated random defects

In this section, we compiled results for several simulated diamond moth-eye surfaces with statistical non-uniformity introduced to simulate a series of topological defects. The topological parameters described (distribution or height, radius and packing defects) in Chapter 3 are simulated to determine the sensitivity of the moth-eye surface's optical properties to defects. As described in Chapter 3, the periodic boundary conditions are removed (replaced with fixed boundary) to allow translational asymmetry in the texture. The results are considered accurate within the bounds of the solvers specified [53]. The structures' geometry remains that of hexagonal close packing described in Chapter 3, specifically $p_x = 2r$, $p_y = \sqrt{3}p_x$, except for the case of packing defects.

4.2.1 Topological defects

To better understand the effect that different defect parameters have on the optical performance, a parametric study was conducted, with the analysis following the defect parameters developed in Section 3.3.3. The moth-eye surface topology, the mean value, and spatial standard deviation of the features' width have been varied. This produces structures that are locally ideal but lack periodicity due to, e.g., randomly changing pillar heights. The analysis results are depicted in Section 4.3. Due to translation asymmetry, absorbing boundaries are used, as detailed in Chapter 3. In this case, mean transmittance is introduced as a natural quantitative metric used for the evaluation of the topological sensitivity of moth-eye structure surfaces.

Random vacancies, voids and disorder

Three algorithms with varying degrees of spatial disorder were implemented to investigate the effects of vacancies and positional defects. Removal fraction, C , was varied from 5% to 95% for 144 pillar surfaces using the random processes described in Section 3.3.3 to generate the stochastic arrangements of moth-eye structures, with 240 trials used to accumulate statistics on a surface of size $5\mu\text{m} \times 5\mu\text{m}$. In Appendix D, the mean transmission with standard deviation is plotted against the defect metrics discussed in Chapter 3 - mean hexagonal coordination number $|\Psi_6|^2$, normalised mean empty patch size, μ_A and spatial separation over wavelength ρ . It is interesting to note that transmittance initially increases with C in some cases.

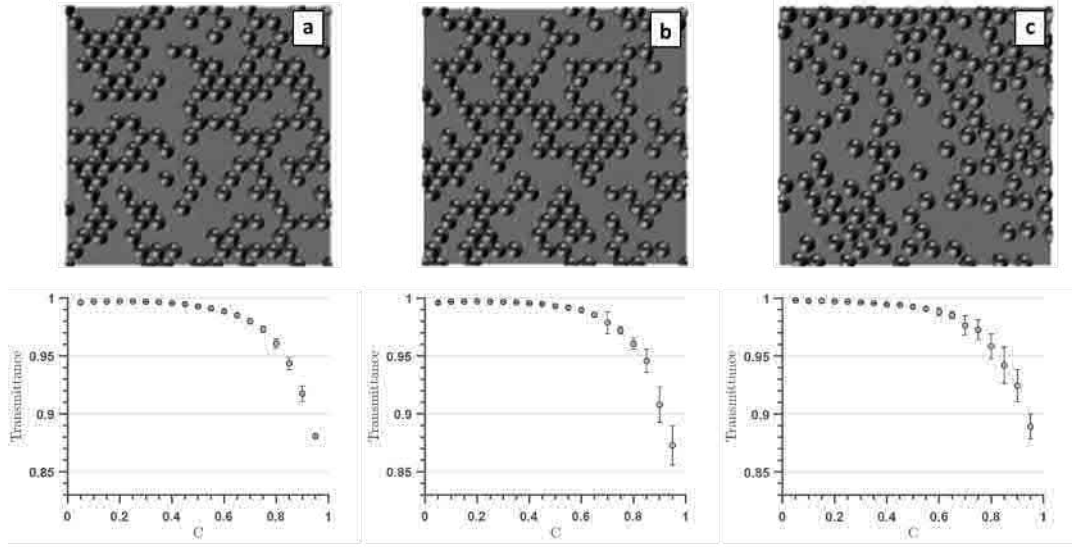


Figure 4.7: Top-down images of $5\mu\text{m} \times 5\mu\text{m}$ simulation domain with 144 moth-eye pillars shown with 50% removed with transmittance plotted against removal fraction, C , for **a)** point removal **b)** patch removal **c)** spatial disorder.

Radius

Figure 4.8 illustrates the calculated transmittance of surfaces with varying half-Gaussian distributions of pillar radius profiles. Radius-variation imperfections are shown in Figure 4.8 as statistical perturbations to the ideal mean radius of $r = 150\text{nm}$ over the range of σ_r from 0 to 50nm . It is noted that deviations of 10nm from the ideal radius of 150nm have little effect on the transmittance.

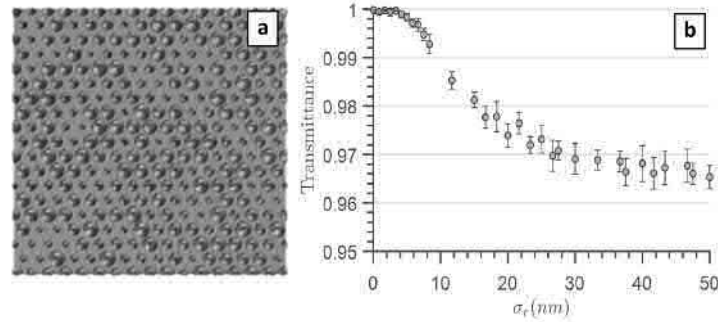


Figure 4.8: **a)** Non uniform surface with $\sigma_r = 35\text{nm}$ **b)** Transmittance as a function of σ_r

Height

Figure 4.9 illustrates the results for non-uniform topology-related defects generated by applying a Gaussian distribution to the moth-eye pillar height. For an ideal mean height of $h = 500\text{nm}$, a statistical perturbation with standard deviation σ_h is used with σ_h changing in the range from 0nm to 150nm . It is interesting to note that transmittance increases as σ_h becomes larger, particularly initially. This bears some similarity to the sinusoidal variation in transmittance for the unit cell (Figure 4.6b); however, here in comparison, the effect of the deviation in height on the transmittance is strongly suppressed and much smaller.

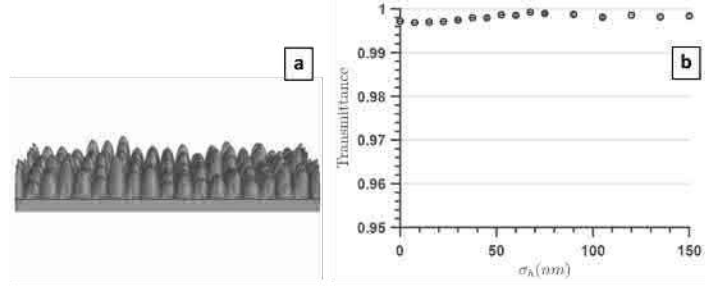


Figure 4.9: **a)** Surface with height deviation from 500nm with $\sigma_h = 120nm$ **b)** Transmittance as a function of σ_h

4.2.2 Profile curvature and random roughness

The defects discussed in this section pertain to local variations in the structure of the moth-eye caused by shape-related defects introduced during the etching process. Perturbations to the shape and dimensions of the characteristic semi-ellipsoid are applied to determine the effect of moth-eye structure shape-related defects on the transmittance through the surface. The effects of top-down etching processes on morphological parameters are also investigated. These are related to the randomness of the local roughness and the flat-tip shape - Gaussian shape of the tip. In this case, due to the local nature of the defect, it can be simulated using a unit cell with periodic boundary conditions. Both deviations from the ideal shape are attributed to non-uniformities in the etching process.

Super-Gaussian shape

The super-Gaussian shape is assumed to be the first deviation from the moth-eye structure's ideal semi-ellipsoidal shape. The super-Gaussian shape is influenced by etching rate and intensity. It is parameterised by Equation 3.6 in Chapter 3, where Ω is varied from 2 to 10. The tip width is used as a physical parameter that can be evaluated in the context of the surface quality and fabrication process. The calculated transmission values for input and output coupling for different values of w are shown in Figure 4.10. All other parameters, including packing, periodicity and size $r = 150nm$, $h = 500nm$ remain unchanged.

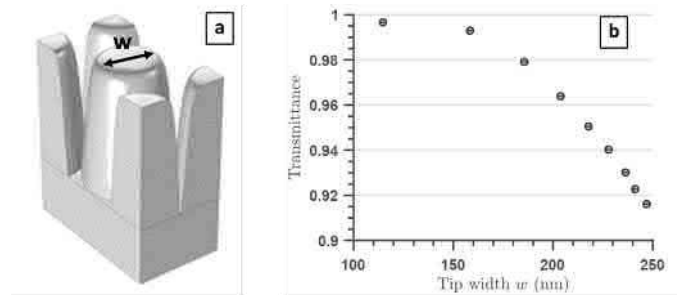


Figure 4.10: **a)** Moth-eye pillar with $\Omega = 4$ and tip width parameter $w = 160nm$ **b)** The effect of a variation in profile geometry on transmittance plotted against tip width.

Roughness

Reactive ion etching-induced surface roughness is a common problem of manufactured surfaces [6]. We model this defect by introducing random roughness to otherwise ideally shaped moth-eye structure, as in Figure 4.11, (with $r = 150nm$ and $h = 500nm$ fixed). The transmittance is expressed as a function

of the root mean square (RMS) of surface roughness. The RMS roughness value combines in a single number the effect of both density and relative intensity of defects, simulated as random noise applied to the structure shape of the ideal moth-eye pillar profile. A gradual decrease in the total transmittance, from 1 to 0.95, of moth-eye structure is observed as RMS roughness is varied from 0 to 40nm. When RMS roughness is increased further, to 60nm, a sharp decrease in the total transmittance of the moth-eye structure is observed.

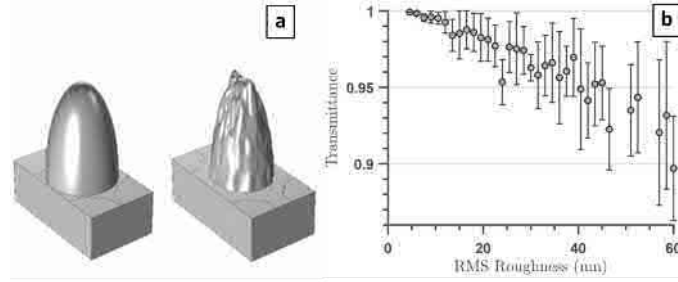


Figure 4.11: RIE-induced surface roughness: **a)** application of random roughness to the ideal shape moth-eye structure ($h = 500\text{nm}$ and radius $r = 150\text{nm}$), with RMS roughness equals 0nm (left) and 32nm (right) **b)** Average transmittance with standard deviation plotted as a function of RMS roughness (nm).

4.3 Discussion: Transmission sensitivity to statistical deviation

The sensitivity of the transmittance is summarised below based on the results of the probabilistic parameter exploration of defects from Section 3.3.3 affecting the morphology and topology of the moth-eye surface.

For super-Gaussian profiles with increasingly flat-top shapes, seen in Figure 4.10, the transmission decreases with further flattening of the super-Gaussian top (increasing exponent Ω). The qualitative metric of tip-flatness is related to the moth-eye structure tip width - the profile sidewalls become steeper, and the curvature of the tip decreases. The transmission varies by 7.2% over a 140nm range of tip width change. Moreover, in the range of w from 190nm to 250nm, transmission decreases linearly with a fast (negative) slope. According to EMT, this corresponds to a more immediate change in n and is also related to the more rapid change in filling factor. These findings demonstrate how the ratio of tip width to base width length is important in transmission values. Moreover, the tip width may be made smaller with little penalty; however, a larger increase beyond 150nm results in significant transmission losses. It is observed that increasing the ratio results in decreased transmittance. This finding is consistent with the effective medium theory [29]. Additionally, this FEM modelling of moth-eye surfaces with varying pillar profiles reinforces that the biomimetic, smoothly tapered design is more optimal than surfaces with more pointed or flat-tipped features [16, 33].

The RMS pillar roughness measurement on the moth-eye pillar in Figure 4.11 indicates that a small degree of roughness is tolerable. Surface roughness increases in direct proportion to defect density and diffusivity of damage on the pillar surface [66]. The results indicate that the moth-eye pillar performance is susceptible to random roughness defects caused by post-etching structural damage when the RMS roughness is larger than 10nm. Transmission is significantly reduced by up to 14% for high RMS values. The significant increase in sensitivity to the pillar's roughness stems from the discontinuity in the smoothly varying n caused by the roughened profile. Despite the pillars' ideal close-packed arrangement, it appears that with an RMS roughness greater than 10nm, the degree of

reflection rapidly increases. The results show that the moth-eye pillar design is highly susceptible to defects that significantly degrade pillar smoothness. Experimentally, sidewall roughness in nanocrystalline diamond surfaces can be reduced to less than $10nm$ RMS, which keeps the moth-eye structures viable [6].

Figure 4.9 shows that variation in pillars' height has no discernible effect on transmission. As the height deviations result in symmetrical structures that are both smaller and taller than the mean height, the effect of non-uniform etching is expected to be negligible. Because the interacting wave's path length is sufficiently long for both the internal reflection and the light-trapping effects to occur, subsequent transmission is unaffected. According to the parameter exploration results, in section 4.2, as long as the resulting etched heights have a Gaussian distribution and the mean is not moved from the ideal, the transmission of the moth-eye surface remains largely unaffected.

Deviation from the ideal radius of $150nm$ has a noticeable effect on the performance of the moth-eye structure. Above standard deviation, σ_r of $10nm$ for radii distribution, transmittance decreases significantly, as seen in Figure 4.8. At the values of σ_r from 0% and 6% ($10nm$), the moth-eye surface is nearly ideal, with transmission exceeding 99%. At σ_r ranging from 6% to 33% the surface is insensitive to non-uniform moth-eye pillar radius-induced scattering. These scattering effects are caused by fabrication process deviations in pillar radius and inter-pillar spacing [67]. As σ_r increases, the distribution of effective transmission becomes wider. This is because the variation between the base of the moth-eye pillar and the base gap size between neighbouring pillars increases. Variation between the air-diamond medium interface and the effective refractive medium, such as discontinuity in the refractive medium, reduces aggregate transmission across the moth-eye surface. However, as the standard deviation of the radius approaches $50nm$, the intensity plateaus, demonstrating insensitivity beyond a degree of variation (around $\sigma_r = 30nm$). At the same time, the transmittance is most sensitive to variations in σ between 10 and $30nm$. Nonetheless, even with a large variation in the pillars' radii, of the order of $50nm$, the transmittance can still be maintained at 97%.

The effective transmission in the presence of random vacancies was determined using a series of randomly generated surfaces with increasing fractions of pillars removed. Figures 4.7 and 4.12 demonstrate that, overall, the system is tolerant to defects in the ordering of the surface. Up to 50% of pillars must be removed from the surface before a noticeable reduction in effective transmission is observed. In general, the decreasing transmittance trend reflects equivalent sensitivities for all three types of removal. Up to a removal fraction of 0.5, the average transmission and standard deviation are nearly unchanged. The moth-eye surface retains a high degree of order in this range, and transmittance remains insensitive to such change. This includes point removal, patch removal, and spatial disorder. Thus, irrespective of the packing quality, the pillars can be arranged in such a way that the surface retains the properties of a smoothly varying spatial refractive index while minimising surface reflections. When the removal fraction exceeds 0.5, the transmittance monotonically decreases with a large (negative) slope. Here $C = 50\%$ appears to be a critical fraction of moth-eye pillar removal beyond which there is a catastrophic degradation of the transmittance of the surface.

The effect on incident light is somewhat different if the defect areas contain densely packed pillars than when the spacing is sparse. For example, the uncertainty in the transmission is more tightly bound for the point removal and patch removal processes. The difference is due to the increased positional randomness in the surface generated by the molecular dynamics simulation described in Chapter 3. This allows for spatial freedom in the location of moth-eye structures and thus clustering, which in

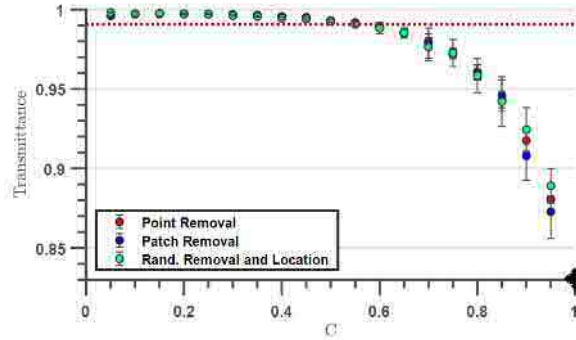


Figure 4.12: Plot of average transmission vs moth-eye pillar removal fraction, C , for three removal methods. The red line indicates optimal transmittance of 0.99. The diamond marks the transmittance of untextured diamond, 0.83.

turn produces a high degree of variation in the local packing density and order (Appendix D). As a result, the way structures are packed into or around untextured areas becomes critical, so that the decrease in transmissivity caused by random structure removal appears to be most significant.

As seen in Figure 4.12 while the removal fraction approaches one, the transmittance is spread over a wide range for all three removal types. The spread in transmittance is attributed to pillar clustering on surfaces with a high removal fraction. When C is large, and structures are sparse, transmission is reduced; however, transmission is less affected when C is large and pillars are clustered. The following factors contribute to the decreased transmittance:

1. *The surface may no longer appear as a graded refractive index in regions where a large number of cells have been removed.*
2. *Isolated or small clusters of moth-eye structures may appear as secondary scatterers of rays reflected from the untextured diamond substrate (a scattering regime that is not subwavelength).*

Furthermore, the broad variation in transmittance for this kind of scattering does not correspond to a specific known scattering process, such as Mie or Rayleigh scattering, used to describe the scattering from isolated particles. Instead, the scattering occurs in the system because of fluctuations in the particle assembly, the moth-eye surface, which contains statistical holes and is composed of a disordered arrangement of ordered and highly correlated domains. Almost certainly, the scattering of such an arrangement cannot be described in terms of an approximation of independent-particle scattering [68]. This phenomenon is not within the scope of the study but provides a potential avenue for further investigation.

The application of randomisation in topological parameters may result in a significant enhancement of multiple scattering caused by the random arrangement or random diameter, similar to what is observed in two-dimensional random media [69, 70]. As the randomness in the geometry is not constrained only on the plane perpendicular to the direction of the incident wave, the incident wave is likely to be diffracted and then multiplicatively scattered by the moth-eye structures [69]. Moreover, all three spatial defect cases exhibit a substantial increase in transmission loss as the removal fraction is increased. According to EMT, one would expect the transmittance to decrease as the defect feature grows larger than the wavelength of light. However, it is demonstrated by the above that the sensitivity of transmission to defects is possibly a scattering-related etching or topological effect rather than a pure

interference effect. As a result of these findings, it follows that strong AR behaviour can be maintained only if all types of irregularities that result large areas of untextured surface and the spatial frequencies violating the subwavelength condition are avoided. If high transmission is required, surface roughness is perhaps the most important parameter to minimise.

4.4 Comparison of Simulation with Experiment

In Table 4.1 we make a comparison between two methods of transmittance prediction with experimental measurements by using modelling and input data from experimental moth-eye surfaces. The accuracy of the simulation model and machine learning model is compared to experimental measurements for five sample diamond moth-eye surfaces. The surfaces exhibit defects in etching and deposition through both packing density and the appearance of voids between clusters on the surface. SEM images, taken at different locations on the sample surface, and over a range of magnifications, from 8000x to 40000x, are used to estimate the input statistics for the *COMSOL* and meta-model predictions. *WSxM* and *ImageJ* are used to estimate the mean height and standard deviation of the moth-eye structures for each image.

Preliminary assessment of accuracy and model evaluation is made for the *COMSOL* and machine learning models used. It is noted that images of the experimental sample surfaces were limited, and the height distribution for Samples 4 and 5 was estimated from previous measurements [23]. Thus, these constraints are considered when evaluating the degree of accuracy to predict the transmission of the experimental surface. In consideration of high surface packing density, Sample 4 predictions made with the machine learning model showed a close relationship with the *COMSOL* model and the experimental data. For Sample 5, the discrepancy between simulation, model, and experiment transmission measurement is much greater.

Observations

In the case of Sample 1, the *COMSOL* model and the machine learning model return similar values for the transmittance. Similarly, the results for Sample 2 and 3 agree as well. Thus in the context of these results, the modelling assumptions are self-consistent. However, real surfaces, such as those in Sample 1, may have additional disorder features, including broken structures and regions of multiple layer formations (bilayers). These are not accounted for in either the *COMSOL* or machine learning model. Consequently, it is feasible to expect the experimental measurements to deviate from our modelling in such cases. Appropriately, more sophisticated testing of the consistency of the machine learning model predictions with *COMSOL* for real surface inputs and experimental measurements is required, which will provide a greater assessment of the suitability of modelling validity. Investigation of this provides the opportunity for further development of the modelling approaches.

While there is a larger discrepancy with the experimental measurement of Sample 5, despite similar surface texture, insufficient data from imaging was likely the cause of the higher predictions for the transmittance. This may be attributed to the presence of additional defects that have not been imaged. In comparison, the results for Sample 4 indicate reasonable agreement between the models and experiment. In the case of Sample 5, limited imaging of the surface prevents a reasonable estimation of the proportion of defects attributed to vacancies and voids. Therefore, a small number

Table 4.1: Results of the simulation and GPR model compared to experiments

	Removal fraction C	Mean height μ_h (nm)	Standard deviation in height σ_h (nm)	Mean radius μ_r (nm)	Standard deviation in radius σ_r (nm)
Sample 1	0.09	436	124.2	130	42
	0.08	390	114.5	122	41
Sample 2	0.23	651	81.44	135	19.2
	0.36	639	85.18	131	20.8
Sample 3	0.21	588	76.14	126	25.2
	0.24	624	78.14	132	24.1
Sample 4	0.16	300	-	140	18
	0.12	300	-	140	16.5
Sample 5	0.28	400	-	125	12
	0.39	400	-	130	14
	0.15	400	-	125	12.5

	<i>COMSOL</i> transmittance value		GPR model transmittance value		Experimental Value
Sample 1	0.958	0.949 ± 0.009	0.962	0.9545 ± 0.008	Not measured
	0.940		0.947		
Sample 2	0.991	0.986 ± 0.005	0.984	0.985 ± 0.002	Not measured
	0.982		0.987		
Sample 3	0.995	0.996 ± 0.001	0.997	0.995 ± 0.002	Not measured
	0.997		0.994		
Sample 4	0.988	0.989 ± 0.001	0.982	0.985 ± 0.003	0.988 ± 0.007
	0.990		0.987		
Sample 5	0.985	0.983 ± 0.007	0.975	0.977 ± 0.005	0.965 ± 0.008
	0.976		0.973		
	0.989		0.983		

of simulations is likely not representative of that proportion of the experimental surface with packing defects.

GPR based statistical machine learning improves the simulation's usability by utilising simple topological information readily available from SEM and AFM images. Notably, optimising the model for the surface transmittance is simplified, and variation caused by stochastic features can be successfully and deterministically parameterised, with the defect metrics consistently associated with the transmittance of the surface. It has been demonstrated that using statistical machine learning to model the defects in the topology of diamond moth-eye surfaces; it is possible to predict surface transmittance from simple topological information such as moth-eye pillar location, radius distribution, and height distribution. All of which can be easily obtained from SEM and AFM images. However, it should be noted that this approach is inherently constrained by the number of points used to train the model and the degree of variation reflected in the data.

Further improvement to the machine learning model and the accuracy and applicability would be

gained from a larger set of SEM and AFM measurements. This is exemplified by the fact that the machine learning model does not take into account the pillar locations, while the *COMSOL* model does. The underlying assumption is that the statistical approximation of the surface texture is sufficient to estimate the transmittance of the entire moth-eye surface. The contrast in the results for Samples 4 and 5 suggests the limitation of such an assumption but it is not conclusive. A larger test of sample data, not accessible at this time, is required to investigate this further. For surfaces where the defects are primarily deviations in height and radius, the approximation is valid and would require few SEM and AFM measurements. However, in the case of packing defects and vacancies, the number of SEM images sampled would be much greater in order to determine a statistically significant sample that minimises the occurrence of edge cases in which a large fraction of pillars are removed from the surface, which would result in a lower representative transmittance.

4.5 Summary

Due to the extremely high transmission of the ideal moth-eye surface, it is expected that this optimisation will be sensitive to defects. Irrespective of the details of the removal process, between 50% and 90% pillar removal fraction, there is a significant degree of sensitivity in the transmittance due to packing defects. In contrast, while maintaining a high packing density, morphological profile defects affecting the tip width, roughness, or base radius of the moth-eye pillar can reduce transmittance by 5% to 14%. However, there is little sensitivity to defects from deviation in height. Indeed, the results demonstrate that while high transmittance is less susceptible to random spatial and orientation defects, it is still susceptible to radius and shape defects for low removal fractions. Moreover, controlling the order of the surface's structure is not necessarily practical as the number of pillars is designed with a high degree of entropy—as an analogy, the pillars can be thought of as identical particles. As the entropy of the pillars' arrangement on the surface increases when the removal fraction is above 0.5, transmission decreases proportionally. The diamond moth-eye surface maintains a high level of optical performance in the presence of significant topological degradation, and consequently, surfaces such as these can sustain function despite significant departures from ideally (symmetrically) arranged structures.

From a fabrication standpoint, the analysis identifies fabrication processes that may require close monitoring in order to account for defect features that significantly affect transmittance. Belcourt *et al.* demonstrated previously that the height and shape of surface structures are dependent on the significant plasma parameters used during etching, including mean ion energy, pressure, gas composition, and treatment time [23]. Sensitivity analysis revealed that defects affecting the morphology of the moth-eye pillars, specifically, tip width, roughness, and base radius, must be minimised. It is clear that controlling the etching process to maintain the gap between nano-spheres, tip width, and roughness to values close to the ideal will keep the values of transmittance above the desired threshold. When the removal fraction C is less than 50%, the effects due to point defects, small patches, positional disorder, and clustering are similar. Only in the case of significant deposition errors, where the removal fraction is greater than 50%, is it necessary to consider the control over and individual influence of each defect. For example, some defects to consider may be cracks that form during the drying process of the films that introduce disorder into the colloidal crystal packing density. The parameters discussed in this section can be used to guide the fabrication process to minimise systematic and random defects that affect the packing and density of pillars on the surface.

Chapter 5

Conclusion and outlook

In this work, we have numerically demonstrated the sensitivity of transmittance to fabrication induced defects on diamond moth-eye surfaces using a variety of quantitative techniques that complement experimental development. Defects of macroscopic and microscopic magnitude were observed in nanosphere lithography-prepared samples. A simulation model was developed based on SEM images of typical samples to describe the defects in moth-eye anti-reflective surfaces. We used *MATLAB* and *COMSOL*, in combination with image processing techniques, to generate diamond moth-eye surfaces with fabrication-induced defects and estimate the transmission through the surface. The *COMSOL* model robustness was validated numerically and experimentally.

The simulation used a stochastic distribution model to account for defect parameters such as:

- Deviation in tip width
- Roughness to moth-eye pillar profile
- Deviation in pillar the base radius
- Deviation in pillar height
- Deviation in packing density and order

Consequently, it was possible to quantify the role of defects relating to the topology and morphology of moth-eye surfaces on the transmittance and anti-reflective properties. The analysis indicates that defects can be reasonably controlled to prevent the transmittance from degrading below 99% for an optimised moth-eye surface with pillar radius equal to $150nm$ and height equal to $500nm$. Specifically, we found that:

- If greater than 99% transmittance is required, the pillar roughness must be maintained below $10nm$.
- If flat-topped structures are produced, such that the tip width approaches the size of base diameter, transmittance decreases up to 7.2%.
- For radii less than $150nm$ and heights greater than $500nm$ the most crucial parameter to control was the spacing between the moth-eye pillars.
- The deviation in the moth-eye pillar base radius cannot be more than 6% if a transmission of greater than 99% is required.
- Large variations in height can be tolerated without adversely affecting transmission for radii consistent with the subwavelength condition, such as $355nm$.
- High surface transmittance is most sensitive to "local" roughness, whether it is packing density defects or roughness of pillar surface, and largely insensitive to orientational order or minor

morphological defects.

- Up to 50% of the moth-eye surface can remain untextured or contain missing pillars and maintain high transmittance.

The results of this study support that the influence of defects on transmittance is measurable and predictable using simulation and modelling. The hierarchy of defects (most significant to least significant) is:

- Deviation in radius
- Deviation in packing density and average spacing
- Variation in moth-eye pillar roughness and tip width

This work developed two methods for estimating transmittance. The first method utilised location, radius, and height data from SEM and AFM images to generate a COMSOL model of the surface. The second approach involved processing the SEM image to extract input parameters for the machine learning fitted model used to estimate transmittance. The model accurately predicted transmission with a maximum error of 0.41%. The agreement between predicted and observed results with small residuals demonstrates that in these cases, the *COMSOL* or machine learning model can provide a reasonable estimate for imaged surfaces. This is a significant accomplishment because it enables near-instant monitoring and optimisation of the manufacturing process. Additionally, the faster machine learning fitted model does not sacrifice accuracy. With adequate input data, the proposed model may be endorsed as a valuable tool for simulating diamond moth-eye surfaces with defects. Finally, the analysis identifies various types of surface defects caused by etching as a significant problem that must be closely monitored throughout the manufacturing process. This is encouraging for practical efforts because it demonstrates the robust anti-reflective properties of moth-eye surfaces as well as the feasibility of manufacturing them via scalable and rapid processes.

Future scope of the work

Several additional anti-reflective properties can be investigated to determine the role of defects on the performance of diamond moth-eye anti-reflective surfaces. These include oblique angle of incidence, broadband high transmittance, and polarisation independence. Thus, a future extension for the proposed model could be calculating and measuring angle-resolved scattering data. As seen in Figures 4.8 and 4.11 transmittance rapidly decreases with a wide range of uncertainty. In practice, this may involve measuring the degree of diffuse scattering. This is relevant also to Figure 4.12 where exposed clusters of moth-eye pillars or regions of vacancies for certain packing defects may influence scattering driven losses to the transmittance of the surface. Alternatively, future work could be directed towards investigating how the etching parameters affect the roughness of the moth-eye pillar profile and global surface. Further improvements could be made in modelling the distribution of the pillars under varying defect conditions. It would be beneficial to use more sophisticated methods of modelling colloidal monolayer formation that are implemented in the work of Abdellatif *et al.*, where a generative algorithm is used to simulate the chaotic aggregation, and nucleation of colloidal monolayers [71], including domain formation as well as voids. Finally, additional research could investigate more robust machine learning models.

Bibliography

- [1] M. Moayedfar and M. K. Assadi. In: *Reviews on Advanced materials science* 53.2 (Feb. 2018).
- [2] S. Chattopadhyay et al. In: *Materials Science and Engineering: R: Reports* 69.1-3 (June 2010).
- [3] S. V. Raghu and R. Thamankar. In: *ACS Omega* 5.37 (Sept. 2020), pp. 23662–23671.
- [4] H. Kikuta et al. In: *Optical Review* 10.2 (Mar. 2003), pp. 63–73.
- [5] H. K. Raut et al. In: *Sci* 4 (2011), p. 3779.
- [6] M. P. Hiscocks et al. In: *Diamond and related materials* 17.11 (2008), pp. 1831–1834.
- [7] P. Forsberg and M. Karlsson. In: *Diamond and Related Materials* 34 (Apr. 2013), pp. 19–24.
- [8] A. Dhawan et al. In: *Small* 7.6 (Feb. 2011), pp. 727–731.
- [9] A. Ahnood et al. In: *Advanced Biosystems* 4 (Oct. 2020).
- [10] I. Aharonovich et al. 2011.
- [11] D. Bouhafs. In: *Solar Energy Materials and Solar Cells* 52.1-2 (Mar. 1998), pp. 79–93.
- [12] K. Han and C.-H. Chang. In: *Nanomaterials* 4.1 (2014), pp. 87–128.
- [13] Z. Han et al. In: *Progress in Materials Science* 103 (June 2019), pp. 1–68.
- [14] D. S. Hobbs and B. D. MacLeod. In: ed. by G. J. Exarhos et al. SPIE, Oct. 2007.
- [15] L. W. Chan et al. In: *Bioinspiration & Biomimetics* 13.4 (May 2018).
- [16] S. A. Boden and D. M. Bagnall. In: *Progress in Photovoltaics: Research and Applications* 18.3 (May 2010), pp. 195–203.
- [17] B. K. Mousavi et al. In: *Journal of Applied Mathematics and Physics* 07.12 (2019).
- [18] T. Kiseleva et al. In: *Journal of Physics: Conference Series*. Vol. 217. 1. IOP Publishing. 2010.
- [19] Y.-F. Huang et al. In: *Nature nanotechnology* 2.12 (2007), pp. 770–774.
- [20] E. Granados et al. In: *Optics Express* 25.13 (June 2017), pp. 15330–15335.
- [21] A. A. Bushunov et al. In: *Laser & Photonics Reviews* 15.5 (2021).
- [22] Z. Han et al. In: *Biosurface and Biotribology* 2.4 (Dec. 2016), pp. 137–150.
- [23] J. Belcourt. MSc Thesis. University of Melbourne, 2018.
- [24] K. Ganesan et al. In: *Biomaterials* 35.3 (2014), pp. 908–915.
- [25] N. Vermeulen et al. In: OSA, 2018.
- [26] A. Muhr et al. In: *2018 IEEE Research and Applications of Photonics In Defense Conference*. IEEE, Aug. 2018.
- [27] J. F. DeNatale et al. In: *Journal of Applied Physics* 71.3 (Feb. 1992), pp. 1388–1393.
- [28] T. Choy. In: *Oxford University Press* 165 (2015).
- [29] E. B. Grann et al. In: *Journal of the Optical Society of America A* 12.2 (Feb. 1995), p. 333.
- [30] C. L. Haynes and R. P. V. Duyne. In: *The Journal of Physical Chemistry B* 105.24 (May 2001).
- [31] S. Das et al. In: *Surface and Coatings Technology* 319 (June 2017), pp. 353–358.
- [32] L. O. L. Cunff et al. In: *Nano Select* 2.1 (Nov. 2020), pp. 140–145.
- [33] R. H. Siddique et al. In: *Nature communications* 6.1 (2015).
- [34] V. Lotito and T. Zambelli. In: *Advances in Colloid and Interface Science* 246 (Aug. 2017).

- [35] P. Stavroulakis. PhD Thesis. University of Southampton, 2012.
- [36] T. Bora et al. In: *International Journal of Smart and Nano Materials* 10.2 (Nov. 2018).
- [37] K.-H. Kim and Q.-H. Park. In: *Scientific Reports* 3.1 (Jan. 2013).
- [38] D. Lehr et al. In: *Optics Express* 18.23 (Oct. 2010), p. 23878.
- [39] P. Colson et al. In: *Journal of Nanomaterials* 2013 (2013), pp. 1–19.
- [40] A. T. Cannistra. PhD thesis. The University of North Carolina at Charlotte, 2011.
- [41] R. Leitel et al. In: *Applied Optics* 47.13 (Dec. 2007), p. C143.
- [42] T.-W. Weng et al. In: *Nanophotonics* 6.1 (Jan. 2017), pp. 299–308.
- [43] D. Mawet et al. In: *The Astrophysical Journal* 633.2 (Nov. 2005), pp. 1191–1200.
- [44] H. Imada et al. In: SPIE, Sept. 2012.
- [45] D. Sabui et al. In: SPIE, Aug. 2020.
- [46] M. M. Elsayy et al. In: *Optics Express* 29.19 (2021), pp. 29887–29898.
- [47] A. Ishimaru. In: *Proceedings of the IEEE* 79.10 (1991), pp. 1359–1366.
- [48] D.-H. Ko et al. In: *Soft Matter* 7.14 (2011), pp. 6404–6407.
- [49] D. H. Raguin and G. M. Morris. In: *Applied optics* 32.7 (1993), pp. 1154–1167.
- [50] T. Mollart and K. Lewis. In: *physica status solidi (a)* 186.2 (2001), pp. 309–318.
- [51] G. Turri et al. In: *Optical Materials Express* 7.3 (2017), pp. 855–859.
- [52] O. Glushko et al. In: *Optics express* 18.7 (2010), pp. 7101–7107.
- [53] COMSOL. URL: <https://www.COMSOL.com/wave-optics-module>.
- [54] H. Kim et al. In: *Nanoscale* 12.37 (2020), pp. 19461–19469.
- [55] I. Horcas et al. In: *Review of Scientific Instruments* 78 (2007), p. 013705.
- [56] M. Schulze et al. In: *Optics express* 20.16 (2012), pp. 18348–18355.
- [57] A. Lagae et al. In: vol. 29. 8. 2010, pp. 2579–2600.
- [58] C. Moore et al. en. In: *R. Soc. open Sci* 3.5 (May 2016), p. 160125.
- [59] A. Andrew. en. In: *Kybernetes* (2003), 628, 0–521–64298–1.
- [60] C. E. Rasmussen and C. K. I. Williams. In: *Neural Networks* (2006).
- [61] D. Xiao et al. en. In: *IEEE Antennas Wirel. Propag. Lett* 19.12 (2020), pp. 2403–2407.
- [62] C. Hu et al. en. In: *IEEE Photonics J* 11.4 (2019), pp. 1–12.
- [63] H. Sai et al. In: *Progress in Photovoltaics: Research and Applications* 15.5 (2007).
- [64] B. K. Nayak et al. In: *MRS Online Proceedings Library (OPL)* (2008).
- [65] S. Marelli and B. Sudret. In: *Vulnerability, uncertainty, and risk: quantification, mitigation, and management*. 2014, pp. 2554–2563.
- [66] R. J. Davis and P. Jha. In: *Journal of Vacuum Science & Technology B: Microelectronics and Nanometer Structures Processing, Measurement, and Phenomena* 13.2 (1995), pp. 242–246.
- [67] C. Y. T. Huang et al. In: *Nanotechnology* 31.30 (2020).
- [68] S. Durant et al. In: *JOSA A* 24.9 (2007), pp. 2953–2962.
- [69] X. Ruan and M. Kaviany. In: *Microscale Thermophysical Engineering* 9.1 (2005), pp. 63–84.
- [70] H. Bao and X. Ruan. In: *Optics letters* 35.20 (2010), pp. 3378–3380.
- [71] S. O. Abdellatif et al. In: *Appl. Opt.* 59.33 (Nov. 2020), pp. 10432–10440.
- [72] P. Monk et al. Oxford University Press, 2003.

Appendix A

Finite Element Modelling

For complicated geometries with mixed boundary conditions, Maxwell's equations can be solved using FEM [72]. However, there is no closed-form solution to the problem in the absence of an underlying symmetry that allows for two-dimensional reduction. This is because the effective medium theory description of sub-wavelength gratings becomes significantly more complicated as a result of the coupling of the parallel and perpendicular electromagnetic field components at boundaries.

FEM is a rigorous full-field technique for modelling optical systems based on frequency. The geometry used in FEM is discretised to represent the shape and size of the surface structures [72]. It calculates the electric and magnetic field strengths over the entire computational domain. The domain is partitioned into finite elements or tetrahedral meshes, and the field strengths are calculated at the mesh vertices. Electric and magnetic fields are represented by time-harmonic complex vectors, with their time dependence defined by $\exp(-i\omega t)$ [12]. To characterise a material's anisotropic properties, optoelectric properties, permittivity, and permeability can be expressed as tensors [12].

Maxwell's equations in the harmonic regime are:

$$\nabla \times \mathbf{E} = i\omega\mu_0\mu\mathbf{H} \quad \nabla \times \mathbf{H} = -i\omega\epsilon_0\epsilon\mathbf{E} \quad (\text{A.1})$$

where ω , ϵ_0 , ϵ , μ_0 , μ are frequency, vacuum permittivity, medium permittivity, vacuum permeability and medium permeability respectively. In matrix form, these equations are arranged by FEM as:

$$\underline{A}.\underline{x} = \underline{b} \quad (\text{A.2})$$

This is a general representation of the discretised Maxwell equations as a linear system of ordinary differential equations where: A is a sparse, symmetric square matrix, x denotes electric and magnetic fields; b denotes a known as electric and magnetic fields vector derived from the boundary conditions and the source excitation.

Appendix B

Defect Metrics

In order to quantify the simulated defects, a set of metrics are defined to measure the statistics of the deviation of the moth-eye surface texture from the ideal texture. The metrics, shown in Table B.1, are calculated from the (x, y) coordinate data from the simulation domain for the pillars on the moth-eye surface, which are returned from the *MATLAB* surface generation script and may also be extracted using the image processing algorithm developed in Section 3.3.3.

Table B.1: Metrics used to measure the statistical deviation of the moth-eye structure from the ideal structure.

Parameter	Symbol	Expression	Description
Global hexagonal orientational order parameter [34]	$ \Psi_6 ^2$	$\psi_6^j = \frac{1}{z_j} \sum_{m=1}^{z_j} e^{6i\theta_{jm}}$ $ \Psi_6 ^2 = \left \sum_{j=1}^N \psi_6^j \right ^2$	$ \Psi_6 ^2$ equals one for a hexagonal ideally closed packed 2D surface and approaches zero for a surface with no observable hexagonal order. N is the total number of particles, z_j is the co-ordination number of particle j , m labels its neighbours, θ_{jm} is the angle of the line between the center of particle j and each of its nearest neighbors with respect to a reference axis.
Normalised mean patch size	μ_A	$\mu_A = \frac{\sigma_{A_i}}{(n-1)}$	The mean empty patch size for an untextured area of the moth-eye surface where no pillars are present.
Normalised patch size standard deviation	σ_A	$\sigma_A = \sqrt{\frac{\sum (A_i - \mu_A)^2}{(n-1)}}$	The standard deviation in empty patch size for an untextured area of the moth-eye surface where no pillars are present.
Normalised Average separation (nm) over wavelength	ρ	$\frac{d}{\lambda}$	The average separation between moth-eye pillars

Appendix C

Machine Learning Model

Performance results

The table below summarises the mean absolute error (MAE) and root mean square error (RMSE) of the GPR model with various kernels.

Table C.1

Kernel	MAE	RMSE
Exponential	0.0023	0.0038
Rational Quadratic	0.0030	0.0048
Mattern	0.0031	0.0049
Squared Exponential	0.0031	0.0049

As illustrated in the preceding table, GPR with an exponential kernel outperforms all other kernels, making it an ideal candidate for the regression problem. To illustrate the performance of GPR with an exponential kernel, the following figure also includes a plot of actual against predicted values.

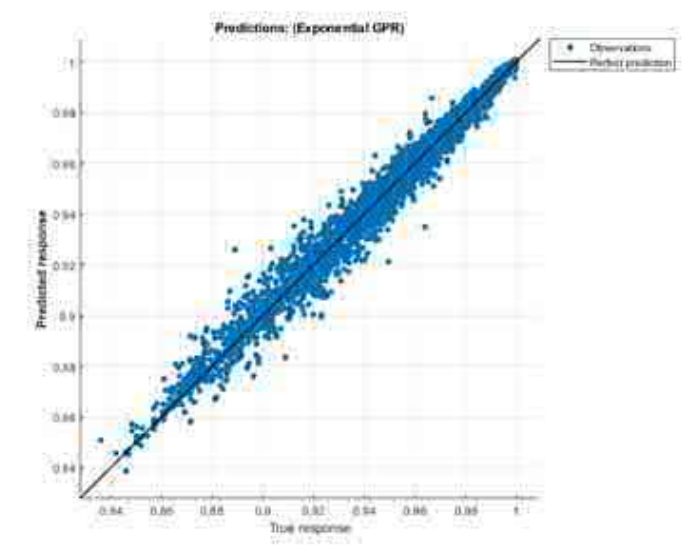


Figure C.1

As can be seen, the predicted and actual values are extremely well matched throughout the interval 0.84 to 1 which corresponds to simulated moth-eye surface transmittance of 84% to 100%.

Appendix D

Sensitivity of transmittance to defect metrics

Figures D.1–D.3 show the sensitivity of the transmission with respect to the defect metrics in various combinations. From Figure D.3a-c), the spread of transmittance observed is attributed to the larger average spacing between pillars. The transmission is most tightly bound for the point and patch removal processes. The contrast with the third process is due to the increased positional randomness in the surface generated by the molecular dynamics, allowing for greater spatial freedom in the location of moth-eye pillars, including clustering. This in turn, produces a high degree of variation in the local packing density and order.

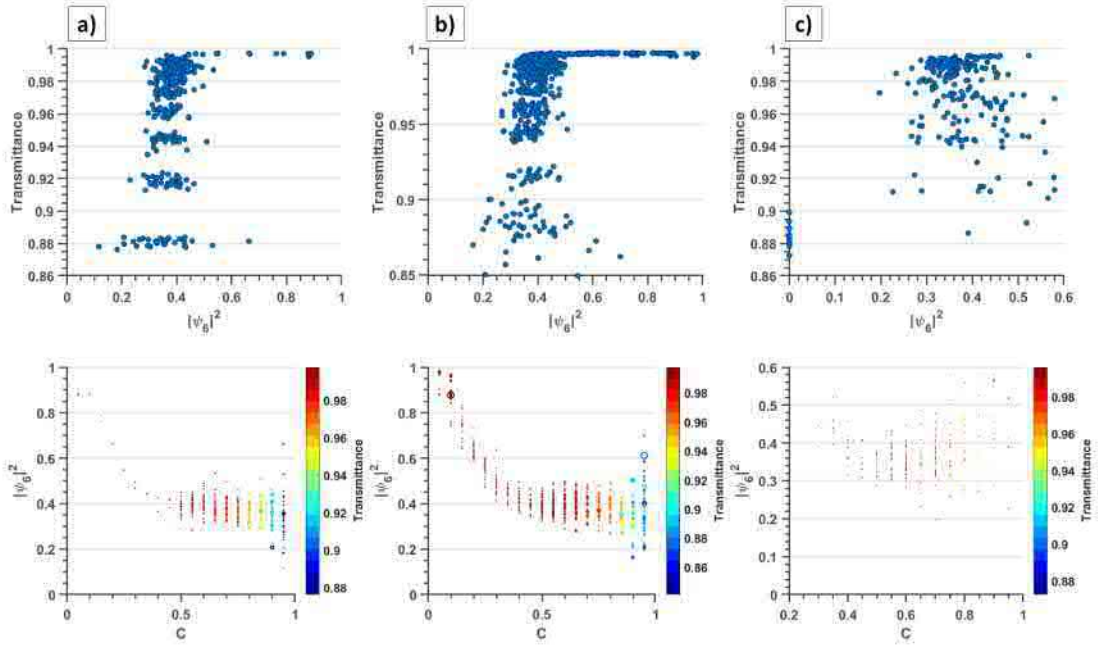


Figure D.1: Top: Transmittance plotted against Global Hexagonal coordination number, $|\Psi_6|^2$, and Bottom: Transmittance plotted as a function of hexagonal coordination number and removal fraction, C for a) Point removal b) Patch removal c) Spatial disorder processes. Dot size indicates degree of variation relative to the smallest point in the transmission for the respective data point.

The hexagonal coordination number, $|\Psi_6|^2$, corresponds to the random arrangement of the moth-eye pillars, was found to be strongly associated with a removal fraction of up to 50%, with a corresponding transmittance near 0.99. Figures D.2a) and D.2b) show that $|\Psi_6|^2$ decays nearly linearly with the fraction of randomly removed pillars for all three removal processes. Figure D.1a-c) shows that the significant decrease in transmittance caused by a high removal fraction is almost completely independent of spatial disorder for the molecular dynamics based process. There is no significant relationship between the coordination of the moth-eye pillars, the removal fraction, and the transmittance for removal fractions greater than 0.5. For a removal fraction, C less than 0.5, the arrangement of the pillars on the surface remains highly ordered. When $|\Psi_6|^2$ is less than 0.5, it corresponds to a generally lower

APPENDIX D. SENSITIVITY OF TRANSMITTANCE TO DEFECT METRICS

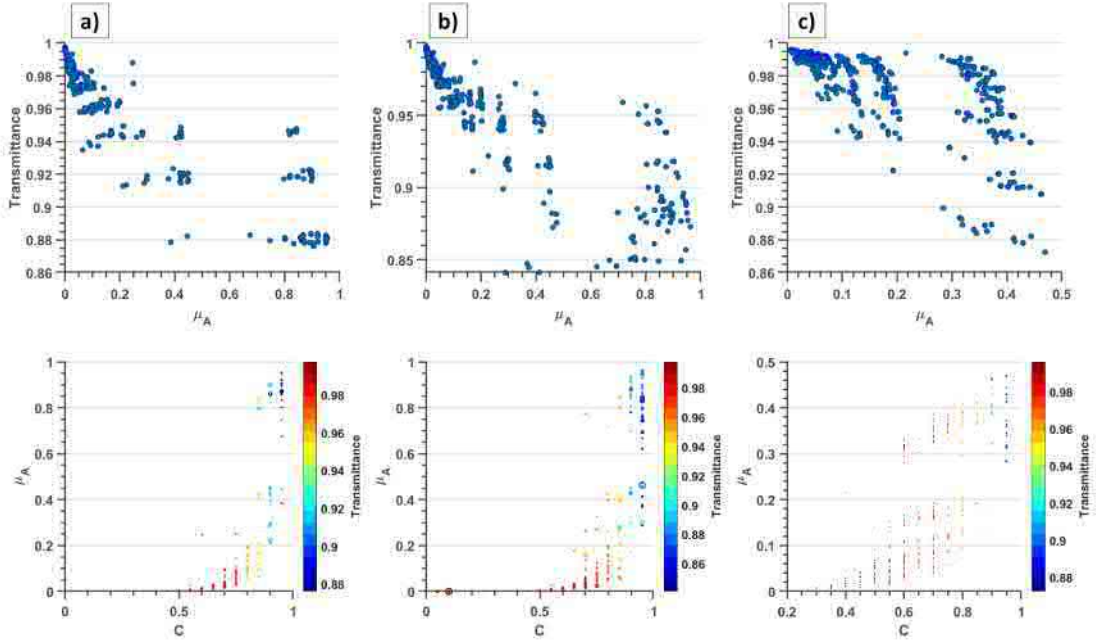


Figure D.2: Top: Transmittance plotted against Normalised Patch size mean, μ_A and Bottom: Transmittance plotted as a function of Normalised Patch size mean and removal fraction, C for a) Point removal b) Patch removal c) Spatial disorder processes. Dot size indicates degree of variation relative to the smallest point in the transmission for the respective data point.

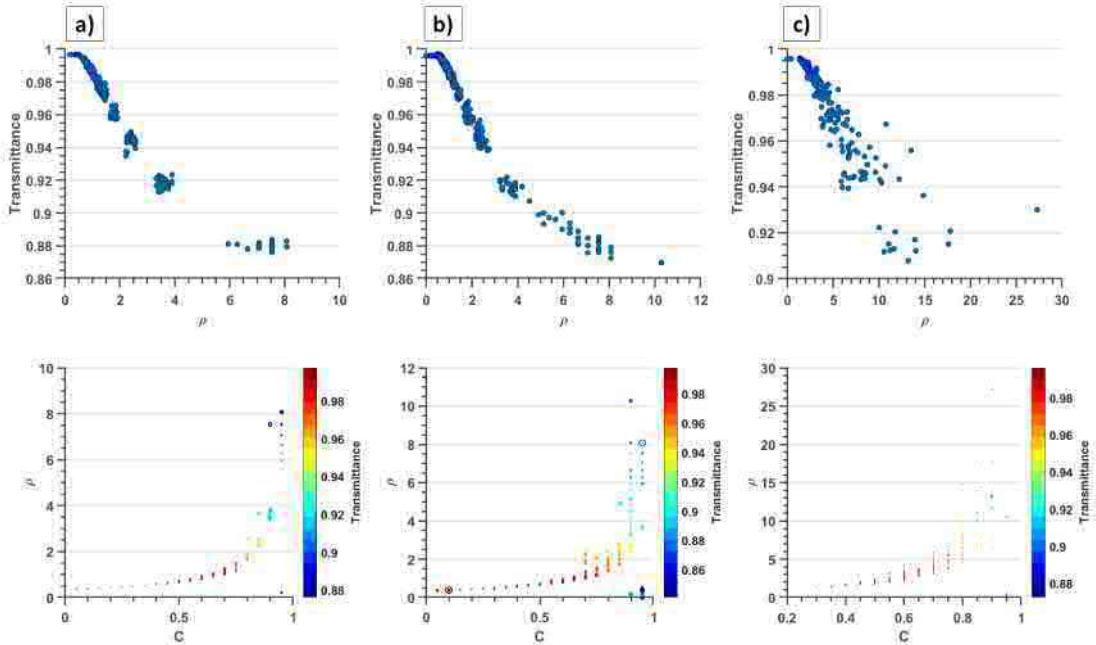


Figure D.3: Top: Transmittance plotted against Average Separation per wavelength, ρ , and Bottom: Transmittance plotted as a function of Average Separation per wavelength and removal fraction, C for a) Point removal b) Patch removal c) Spatial disorder processes. Dot size indicates degree of variation relative to the smallest point in the transmission for the respective data point.

APPENDIX D. SENSITIVITY OF TRANSMITTANCE TO DEFECT METRICS

transmittance but without a strong correlation. Above removal fraction, C , equal to 0, the in-plane structural disorder increases roughly linearly until the structural disorder is far from that of a perfect surface at $C = 0.5$. The observation that transmission saturates at 99% for $C = 0.5$ and not only near $C = 0$ indicates that this transmission value reflects the actual degree of order of the surface and is not an artefact of the finite area of the simulation domain sampled.

Figure D.3 supports the observation that even when some local periods violate the subwavelength condition for structure separation, a random grating can retain a diffraction efficiency comparable to that of a regular grating.

In accordance with the effective medium approximation, Figure D.2b) shows the low spatial separation portion of the transmission curve appears to be almost unaffected by the imperfections in the spacing of pillars. However, because the disordered surface lacks a distinct subwavelength condition, the transmission decreases gradually without a clear boundary until the average separation per wavelength, ρ , is two wavelengths in the case of point and patch vacancy defects, or near 10 wavelengths in the case of random position and removal defects. This corresponds to a significant deviation from the moth-eye surface's regular arrangement and a violation of the subwavelength condition. Compared to point and patch defects generated over a fixed hexagonal lattice, the defects introduced by the random positional and removal process do not have a regular period and thus will generate distinct higher diffraction orders. It is noted that for a small range of random local periods, less than 50%, the defects caused by spatial disorder appear with a transmission efficiency nearly identical to that of the point and patch removal methods.